INORGANIC CHEMISTRY FRONTIERS

RESEARCH ARTICLE

View Article Online
View Journal | View Issue

Cite this: *Inorg. Chem. Front.*, 2026, **13**, 1459

Visible light driven hydrogen bonding assisted complete photocatalytic degradation of selected antibiotics by lanthanide-based metal–organic frameworks

Ruchika Gupta,[a] Shubhangi Majumdar,[b] Pramit K. Chowdhury[b] and Rajeev Gupta *[a]

Metal–organic frameworks (MOFs) could be a promising class of photocatalysts due to their high surface area, framework robustness, and tunable architectures, which enable modulation of their semiconductor properties for enhanced light harvesting and subsequent photocatalysis. In this work, a cobalt-based metalloligand has been utilized to synthesise lanthanide (Ln)-based MOFs (Ln-MOFs). The architecturally engineered Ln-MOFs exhibit significant visible light absorption and support noteworthy photocatalysis for the complete degradation of the selected antibiotics. Both Ln-MOFs enabled complete photodegradation of antibiotics, as supported by their high degradation reaction rates. The Ln-MOFs exhibited remarkably enhanced photocatalytic activity compared to the Co-based photosensitizer. This fact is attributed to an enhanced charge-carrier lifetime for both Ln-MOFs, which was corroborated by the transient absorption spectroscopy, photoluminescence, and electrochemical impedance spectroscopy analyses. These studies, along with the scavenger experiments, helped in establishing the probable mechanism for Ln-MOF-mediated photodegradation. We further illustrate the importance of hydrogen bonding-assisted encapsulation of an antibiotic molecule within the pores of Ln-MOFs, which remarkably improved its photocatalytic degradation. The present visible-light-driven Ln-MOFs are a rare example of photocatalysts exhibiting high efficiency for the complete photodegradation of antibiotics.

Received 5th September 2025,
Accepted 1st December 2025

DOI: 10.1039/d5qi01850a

rsc.li/frontiers-inorganic

Introduction

Photocatalysis is based on the absorption of sunlight, preferably in the visible region, followed by charge separation and further followed by assorted redox reactions.[1–12] Typically, the generation of various reactive oxygen species (ROS) is common under the ambient conditions.[13–15] ROS include $^{\bullet}OH$, $^{\bullet}O_2^-$, and $^1O_2$ that are highly reactive and can efficiently degrade various compounds, including pollutants, into simpler organic and/or inorganic products.[13–18] The best photocatalysts are those that utilize the visible part of the solar spectrum and cause complete photodegradation of organic pollutants to the simplest products, such as water and gases (CO_2, N_2, *etc.*).[1–12,16–18] The designing of an appropriate photocatalyst is essential to achieve meaningful photocatalytic efficiency.[1–15] The semiconductor materials, including metal oxides (TiO_2, Fe_2O_3, and ZnO), metal sulphides (CdS and ZnS), and metal phosphides (CoP, Cu_3P, and FeP), are some of the most-studied photocatalysts.[19–21] However, the photocatalytic efficiency of such materials is primarily limited due to their poor visible light absorption ability and quick recombination of the photogenerated electron–hole pairs.[19–24] The other drawbacks include their limited thermal and moisture stability, restricting their reusability, as well as their low electronic conductivity.[19–24] To address these challenges, significant efforts have been directed toward the development of next-generation photocatalysts that are responsive to visible light and offer improved light-harvesting abilities, and thereby enhanced photocatalytic activity.[1–18,25–28] However, both robustness and reusability still remain the major challenges.[25–28]

Metal–organic frameworks (MOFs) are well-established materials renowned for their large surface area, high porosity, tailorable framework structure, and exceptional stability.[29–37] Furthermore, the tunable nature of MOFs, including both inorganic and organic components, is particularly beneficial for the rational structural modulation, and such a feature has been elegantly shown to assist in various applications.[38–42] In particular, MOFs have emerged as a major paradigm in the field of heterogeneous catalysis.[43–45]

[a]*Department of Chemistry, University of Delhi, Delhi 110 007, India.*
E-mail: rgupta@chemistry.du.ac.in; https://people.du.ac.in/~rgupta/
[b]*Department of Chemistry, Indian Institute of Technology, Delhi 110 016, India*

In the search for novel and better rationally designed MOFs, metalloligands have emerged as the strategic building blocks.[46–53] A metalloligand enables the incorporation of a desirable primary metal ion that may have a profound effect on its photophysical properties.[46–57] A suitable combination of an appropriate ligand(s) and a desirable primary metal ion is likely to enable the resultant metalloligand to absorb visible light and initiate charge transport processes.[58–65] As a result, a metalloligand can act as an effective photosensitizer.[58–62] In this context, polypyridyl complexes of second- and third-row transition metals (Ru and Ir) have emerged as promising candidates due to their appealing photophysical characteristics, such as good light absorption capability, long luminescence lifetime, and excellent chemical stability.[25–28,58–65] Consequently, both Ru and Ir complexes of polypyridyl ligands have been extensively studied for their applications as visible-light photocatalysts for water-splitting, dye degradation, and CO_2 reduction.[58–65]

Although catalyst cost is not a significant consideration for fine-chemical and pharmaceutical applications that target high-value products, it is essential to develop Earth-abundant metal-based photosensitizers for large-scale applications such as water remediation.[66,67] Recent studies have shown that coordination complexes of first-row transition metals can also exhibit improved attributes, particularly in terms of their photostability and excited-state redox properties.[68,69] Thus, it would be beneficial to develop photosensitizers based on 3d-series transition metals rather than their precious analogues for visible-light-mediated photocatalysis.[66–69] Moreover, a majority of the examples are devoted to the metal complexes of polypyridyl ligands while exploring their applications under homogeneous conditions.[70–74] Very few reports are known on MOFs based on Ru/Ir-based metalloligands.[58–65] Since MOFs are highly ordered architectures with large surface area, they are likely to serve as excellent heterogeneous photocatalysts with enhanced stability and robustness.[16–18,29–32]

In recent times, due to an accelerated rise of urbanization, water pollution and wastewater treatment have gained global attention.[16–18,75–82] Based on the chemical composition, common water pollutants can be broadly categorized as either inorganic or organic.[75–85] Metal ions and oxyanions are among the major environmental concerns regarding inorganic pollutants.[16–18,75–78,83–85] By virtue of their chemical diversity, organic pollutants comprise a much larger family and include dyes, oils, detergents, polyaromatic hydrocarbons, pesticides, insecticides, herbicides, and pharmaceuticals (*e.g.*, drugs and antibiotics).[86–88] In particular, both heavy use and misuse of antibiotics not only pose environmental pollution challenges but also detrimental effects on ecology and human health and wellbeing.[16–18,75–88]

Conventional wastewater treatment techniques are unable to efficiently eliminate some of these pollutants due to their persistent nature and non-biodegradability.[89–91] In fact, it is significantly more challenging to degrade antibiotics under physiological conditions due to their stable chemical structure and their resistance to hydrolysis and oxidation.[92–94] Antibiotics typically have a much longer half-life than most organic dyes, often persisting for weeks to months (*e.g.*, >30–60 days for fluoroquinolones and tetracyclines). Their concentration in contaminated water can range between *ca.* 1 and 100 μg L^{-1}, which exceeds their permissible limit (*e.g.*, 0.064 μg L^{-1} for ciprofloxacin).[92–94] In contrast, many organic dyes (such as azo dyes) degrade within minutes to hours under photolytic or oxidative conditions, underscoring a substantially greater persistence and environmental concern associated with antibiotics.[92–94] Several treatment methods have been developed for removing antibiotics from the aquatic environment, including adsorption, membrane separation, activated carbon treatment, ozonation, and advanced oxidation processes (AOPs).[16–18,95–98] AOPs include Fenton-like oxidation and photocatalysis.[95–98] The former method can achieve partial removal efficiency for the water-soluble antibiotics, but is not successful for the insoluble ones.[95–98] Semiconductor photocatalysis has attracted immense interest due to its low operational cost, significant efficiency, and utilization of sunlight as a sustainable energy source for degrading pollutants, including antibiotics, under the ambient conditions.[1–15] However, both these methods suffer from a major disadvantage: incomplete degradation, which often generates intermediates as secondary pollutants.[16–18,89–98] Thus, it is essential to develop new photocatalysts for the complete photodegradation of various organic contaminants, particularly antibiotics.

In this work, we present the design and synthesis of two lanthanide-based MOFs (Ln-MOFs): **1-Tb** and **1-Eu**. Both Ln-MOFs have integrated a Co^{3+}-based metalloligand as a photosensitizer within a three-dimensional (3D) MOF architecture. Both Ln-MOFs display noteworthy visible-light absorption and function as remarkable heterogeneous photocatalysts for the complete photodegradation of several antibiotics. The mechanism underlying the photocatalytic reaction was established using transient absorption spectroscopy and detailed photoelectrochemical experiments, which were further supported by scavenger studies and characterization of the photodegradation products. We also illustrate the elegant role played by hydrogen bonding (H-bonding) interactions between the Ln-MOFs and the antibiotics, which remarkably enhance their photodegradation. Several studies, including molecular docking, FTIR spectral analyses, and control experiments involving structural modifications of an antibiotic molecule, are utilized to establish the role of H-bonding interactions. To the best of our knowledge, the present Ln-MOFs represent an unprecedented example of integrating photosensitizer-based molecular systems and H-bonding interactions to develop remarkable photocatalytic systems for visible-light-mediated catalysis.

Experimental

Experimental details are provided in the SI.

Results and discussion

Synthesis and characterization of 1-Tb and 1-Eu

The metalloligand $Na[Co(L^{p\text{-}COOH})_2]$ (**1**) (Fig. S1–S9, SI) offered four biphenylcarboxylic acid groups. Such appended groups have the potential to coordinate with the suitable metal ions.[48–51] The metalloligand **1** on reaction with $Ln(OTf)_3$ (Ln = Tb and Eu) resulted in the formation of one-dimensional (1D) Ln-MOFs **1-Tb** and **1-Eu** (Fig. 1a). The elemental composition of both Ln-MOFs was confirmed by using energy dispersive X-ray (EDX) spectroscopy (Fig. S10, SI). The X-ray photoelectron spectroscopy (XPS) analysis showed that the binding energies of Co $2p_{3/2}$ and $2p_{1/2}$ remain largely unchanged before and after the coordination of the Ln^{3+} ions.[99,100] Such a fact indicates that the oxidation state of the Co ion (+3) remains unaffected in both metalloligand **1** and its Ln-MOFs (Fig. S11–S13, SI). In the FTIR spectra, both Ln-MOFs exhibited strong stretches at 1590–1575 cm^{-1} corresponding to ν_{COO} and $\nu_{C=O}$ groups (Fig. S14, SI). Both **1-Tb** and **1-Eu** also displayed broad ν_{O-H} stretches at 3290–3210 cm^{-1} due to the presence of lattice water molecules, while a strong band at *ca.* 1000 cm^{-1} is indicative of the coordinated DMSO molecules.[101,102]

Both **1-Tb** and **1-Eu** were characterized crystallographically to understand their molecular structures (Fig. 1 and Fig. S15, SI). Details of the crystallographic data collection and structure solution parameters are provided in Table S1 (SI), whereas Tables S2 and S3 (SI) contain the selected bonding parameters. X-ray diffraction analysis revealed that both **1-Tb** and **1-Eu** crystallized in an orthorhombic cell with the *Pbca* space group. The asymmetric unit consists of one metalloligand **1**, one Ln^{3+} ion, four coordinated DMSO molecules, and several lattice water molecules, nine and eight, respectively, for **1-Tb** and **1-**

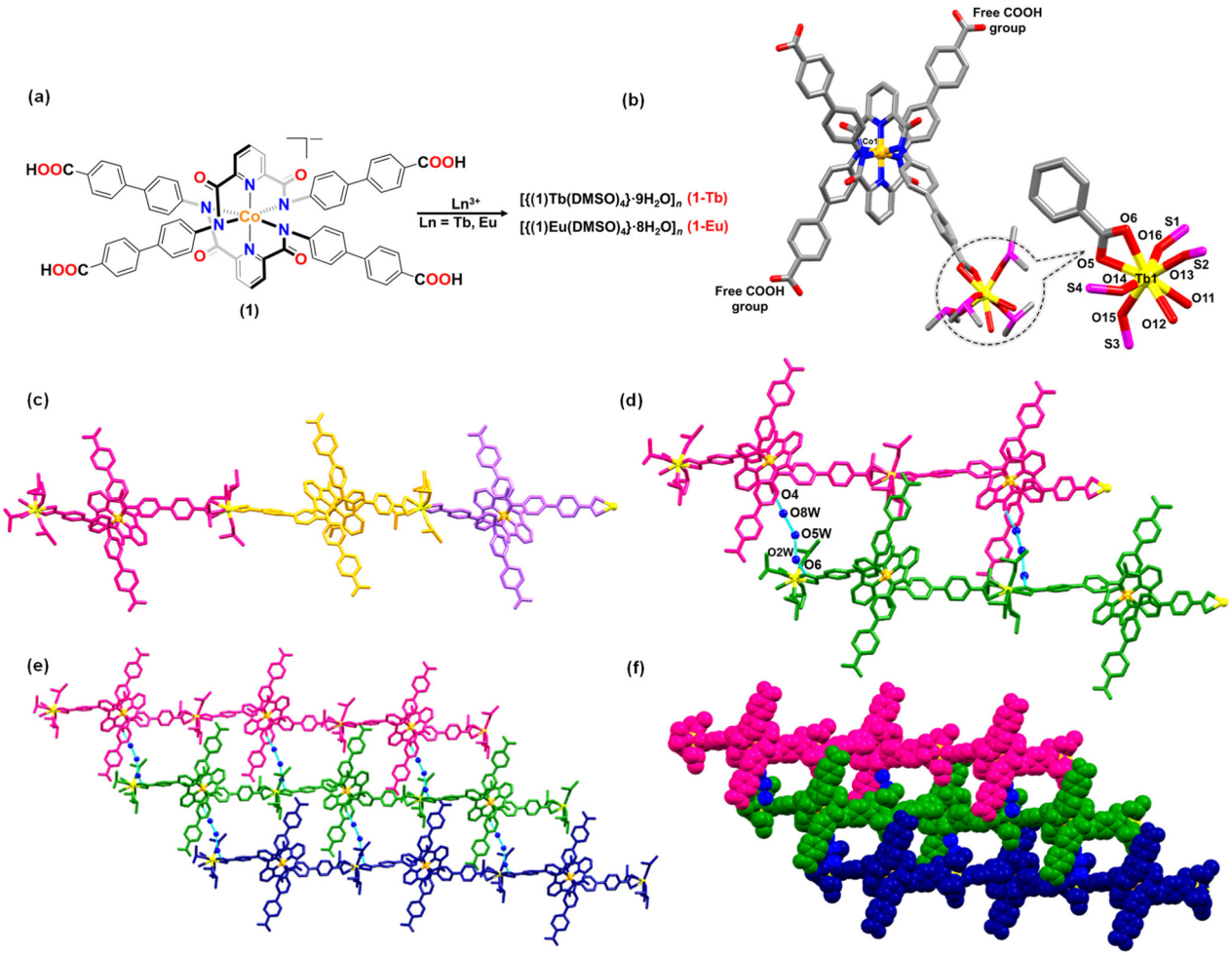

Fig. 1 (a) Preparative route for the synthesis of Ln-MOFs **1-Tb** and **1-Eu**. (b) Stick representation of the crystal structure of **1-Tb**. Color codes: orange, Co; yellow, Tb; pink, S; blue, N; red, O; and grey, C. H atoms and solvent molecules have been omitted for clarity. (c) Crystal structure of **1-Tb** displaying arrangements of metalloligands (shown in pink, golden, and lilac colors) and Tb^{3+} ions generating the 1D chain when viewed along the *c* axis. (d) A section of the crystal structure of **1-Tb** displaying H-bonding interactions between O_{amide} groups and lattice water molecules (shown as blue balls) connecting 1D chains (shown in pink and green colors). (e) A view of the 2D network created due to H-bonding interactions connecting various 1D chains (shown in pink, green, and dark blue colors). (f) Spacefill diagram of **1-Tb** when viewed along the *c*-axis. See Fig. S15, SI, for the crystal structure of **1-Eu**.

Eu (Fig. 1b and Fig. S15a, SI). In both cases, metalloligands are coordinated *via* Ln^{3+} ions to generate 1D chains. In both Ln-MOFs, a metalloligand has an inherent negative charge, while the 2− charge was due to two anionic carboxylate groups. Consequently, the 3− charge is balanced by a Ln^{3+} ion to generate a neutral 1D chain. Importantly, the remaining two arylcarboxylic acid groups remained in their neutral form in both cases and were found to be involved in various H-bonding interactions (*vide infra*).

In both MOFs, a Ln^{3+} ion illustrates an eight-coordinated geometry where two bidentate arylcarboxylate groups, emanating from two different metalloligands, are arranged in a *trans* form, whereas the remaining four sites are ligated by the DMSO molecules. In both cases, only two of the arylcarboxylate groups of a metalloligand coordinate to the Ln^{3+} ions and generate 1D chains (Fig. 1c and Fig. S15b, SI). Such parallel running 1D chains are further connected to each other *via* various H-bonds involving amide and arylcarboxylic acid groups offered by a metalloligand as well as lattice water molecules (Fig. S15c and d, SI). The remaining two free arylcarboxylic acid groups were engaged in various H-bonding interactions and contributed to the formation of an extended 2D structure. Such H-bonding interactions were of a stable nature, a fact evident from the thermogravimetric (TGA) and differential scanning calorimetry (DSC) studies that showed that both Ln-MOFs were stable up to *ca.* 400 °C, after the loss of lattice water molecules (Fig. S16, SI). Both Ln-MOFs exhibited the presence of a porous structure due to the existence of H-bonding interactions between different 1D chains. However, the Brunauer–Emmett–Teller (BET) surface area was very low, in line with the metalloligand-based architectures (Fig. S17, SI).[103,104] Nevertheless, such pores are lined with the hydrophilic groups – lattice water molecules, O-amidic groups, and O-carboxylate groups, as well as hydrophobic groups courtesy of the biphenyl rings. Such a fact provides a unique opportunity for the recognition and binding of a specific analyte within such pores (*vide infra*).[105–107] The PXRD patterns of the as-synthesized samples closely matched those simulated from the single-crystal diffraction analyses, indicating the phase purity of the bulk samples (Fig. S18, SI). The surface morphology of both Ln-MOFs was examined using scanning electron microscopy (SEM), which revealed a block-like morphology for **1-Tb** and a rod-like morphology for **1-Eu** (Fig. 2a and b). Transmission electron microscopy (TEM) analysis further corroborated these observations (Fig. 2c and d), while elemental mapping confirmed the uniform distribution of constituent elements in both Ln-MOFs (Fig. 2e–h).

Light absorption and the band gap structure of Ln-MOFs

The UV-Vis diffuse reflectance spectra (DRS) of **1-Tb** and **1-Eu** revealed absorptions predominantly at 480–510 nm, attributed to the charge-transfer, while a less intense broad band at 686–698 nm is tentatively assigned to the d–d transition of the Co^{3+} ion of metalloligand **1** (Fig. 3a).[46–53] The DRS analyses of both Ln-MOFs revealed strong absorption in the visible region, indicating their potential activity as visible-light photocatalysts.[108–112] Based on the Tauc plot, the band gap energies were found to be 2.42 and 2.58 eV for **1-Tb** and **1-Eu**, respectively.[108–112] Such a fact suggests that both Ln-MOFs present semiconductor-like properties in the visible region (Fig. 3b and c). To gain a better understanding, band structures of both Ln-MOFs were investigated. The Mott–Schottky plots of Ln-MOFs at two different frequencies revealed their typical n-type semiconductor behaviour, owing to the positive slope of the linear plots.[108–112] The flat band positions referring to the lowest unoccupied molecular orbital (LUMO) were determined from the intersection with the values of −0.87 V and −0.94 V *versus* Ag/AgCl (*i.e.*, −0.67 V and −0.74 V *versus* NHE) for **1-Tb** and **1-Eu**, respectively. On account of band gaps determined by Tauc plots and the LUMO potentials estimated by the Mott–Schottky calculations, the HOMO energy levels of **1-Tb** and **1-Eu** were found to be 1.74 V and 1.84 V *versus* NHE,

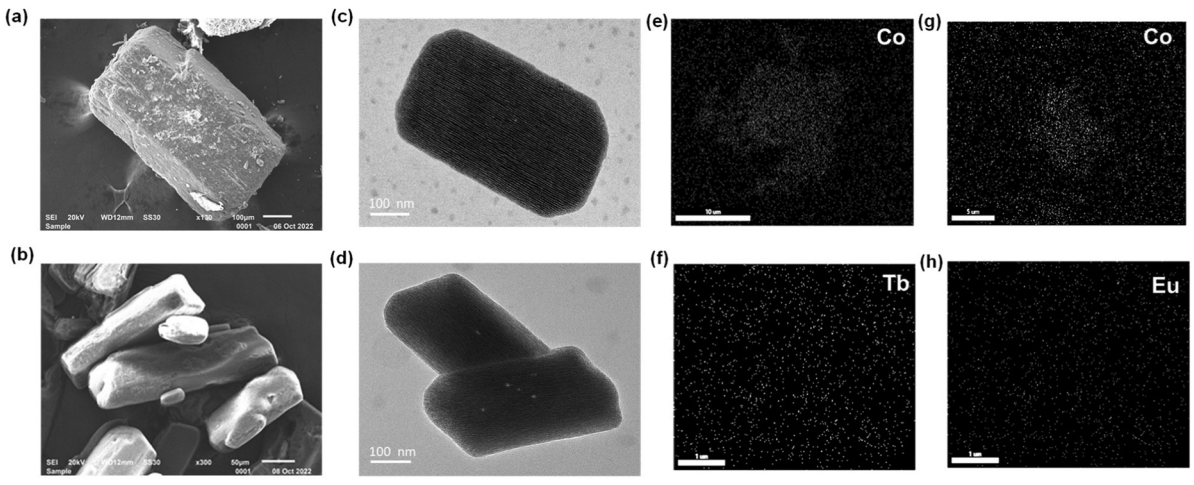

Fig. 2 SEM images of as-synthesized (a) **1-Tb** and (b) **1-Eu**. TEM images of as-synthesized (c) **1-Tb** and (d) **1-Eu**. Elemental mapping for (e and f) **1-Tb** and (g and h) **1-Eu**.

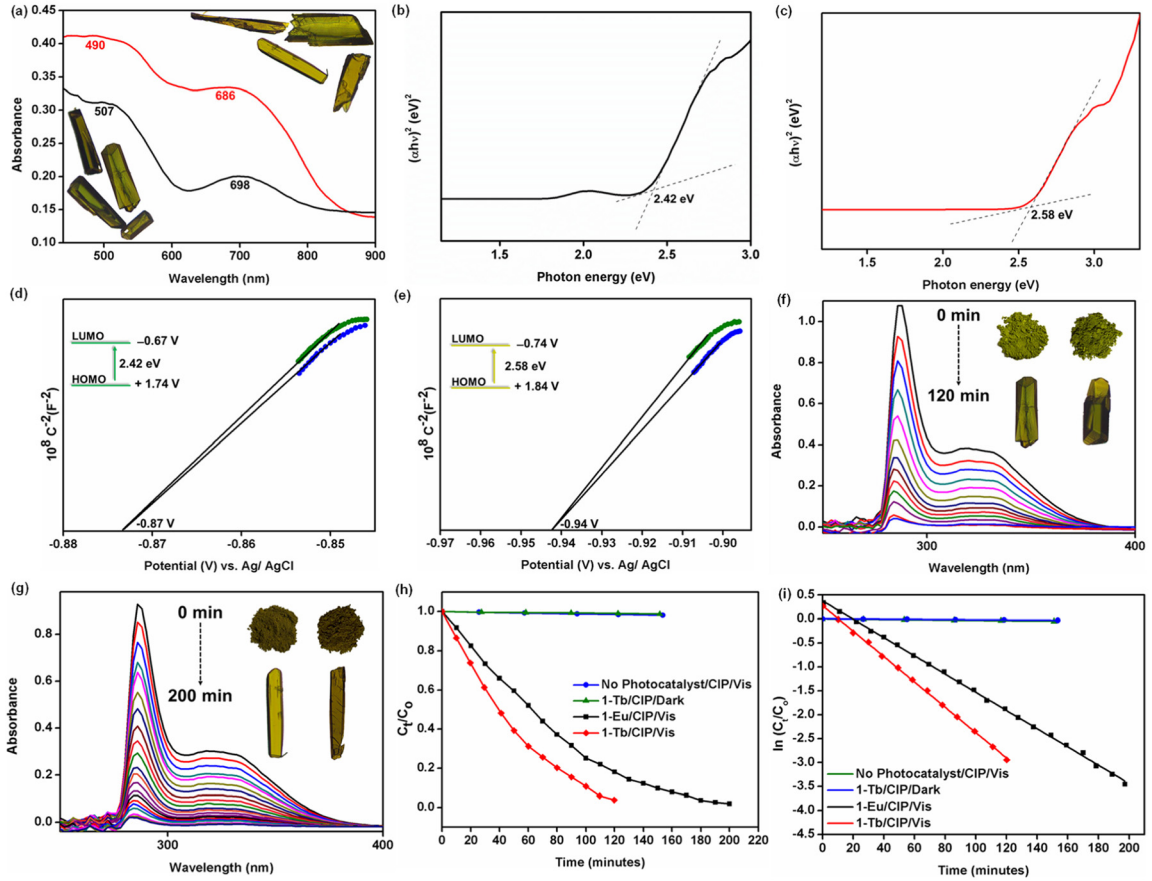

Fig. 3 (a) UV-Vis DRS spectra of Ln-MOFs **1-Tb** (black trace) and **1-Eu** (red trace) (inset: optical images of as-synthesised crystals of **1-Tb** (below) and **1-Eu** (above)). (b and c) Tauc plots for **1-Tb** and **1-Eu**. (d and e) Mott–Schottky plots for **1-Tb** and **1-Eu** at two different frequencies, 0.5 kHz (blue trace) and 1.0 kHz (green trace) (insets: The corresponding HOMO and LUMO levels, potentials *vs.* NHE). (f) Time-dependent (0–120 min at an interval of 10 min) UV-Vis spectra for the photocatalytic degradation of CIP with **1-Tb** under visible-light irradiation (inset: optical images of the powdered form and as-synthesised crystals of **1-Tb** before and after five cycles of CIP degradation). (g) Time-dependent (0–200 min at an interval of 10 min) UV-Vis spectra for the photocatalytic degradation of CIP with **1-Eu** under visible-light irradiation (inset: optical images of the powdered form and as-synthesised crystals of **1-Eu** before and after five cycles of CIP degradation). (h) Photocatalytic degradation of CIP under different conditions. (i) Plot of ln(C_t/C_0) *versus* time representing the first-order kinetics for the degradation of CIP under different conditions.

respectively (Fig. 3d and e). These findings demonstrate that both Ln-MOFs exhibit high visible-light absorption efficiency and are therefore suitable for the photodegradation of organic pollutants, such as antibiotics.

Photocatalytic degradation of antibiotics

Antibiotics can be classified based on their chemical structure, mechanism of action, activity spectrum, or the route of administration.[16–18,109] The most common classification is based on their chemical structure, while the most prevalent subgroups are beta-lactams, sulfonamides, monobactams, carbapenems, glycopeptides, nitrofurans, polypeptides, polyenes, tetracyclines, quinolones, and fluoroquinolones.[109] The following antibiotics from the common categories were selected and investigated for their photodegradation in aqueous solution at pH 7 under visible light irradiation at room temperature (25 ± 1 °C) (Scheme 1): beta-lactams: penicillin G (PG) and amoxicillin (AMX); fluoroquinolones: ciprofloxacin (CIP) and norfloxacin (NOR); nitrofurans: nitrofurantoin (NFT), nitrofurazone (NFZ), and furazolidone (FUR); sulfonamides: sulfaquinoxaline (SQX); and tetracyclines: tetracycline (TC).

Compared to various antibiotics investigated, both Ln-MOFs resulted in the complete degradation of CIP within a short time span (Fig. 3f and g). The absence of visible light completely inhibited the photodegradation. Likewise, negligible degradation of CIP (<1%) occurred in the absence of a catalyst under the otherwise identical experimental conditions (Fig. S19, SI). These observations suggest that the degradation of CIP is a photo-assisted reaction and is catalyzed by the semiconductor photocatalysts, Ln-MOFs. The extent of CIP degradation was *ca.* 98% after 3 h of illumination in the presence of Ln-MOFs. In both cases, the colour of the crystalline sample and the optical images of the crystals did not show any change following the photodegradation experiment (Fig. 3f and g). To understand the reaction kinetics of photodegradation, the experimental data were analysed using the first-order

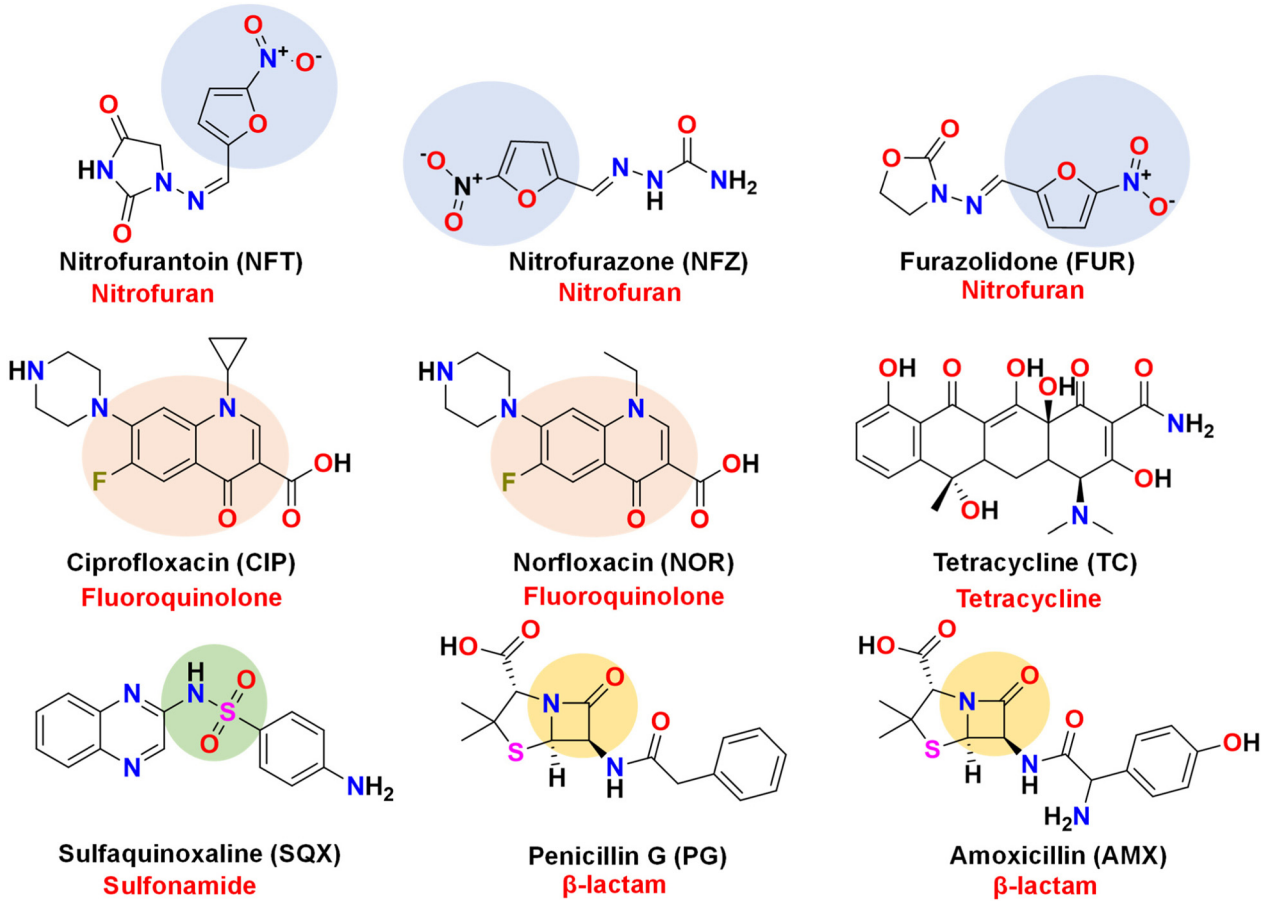

Scheme 1 Molecular structures of the representative antibiotics used for the photodegradation studies by Ln-MOFs.

kinetics.[16–18,52] A linear relationship between $\ln(C_t/C_o)$ and the irradiation time was observed for CIP degradation. Notably, **1-Tb** exhibited a rate constant of 0.0265 min^{-1}, which was nearly 1.4-fold higher than that of **1-Eu** (0.0191 min^{-1}) (Fig. 3h, i and Table S4, SI). Considering the superior photocatalytic performance of **1-Tb**, all subsequent experiments were conducted using **1-Tb** as the semiconductor catalyst.

Impact of pH on the photocatalytic degradation of CIP

The pH of the reaction mixture was measured as a function of time during the photodegradation of CIP (Fig. 4a). The pH was found to decrease significantly with time and reached *ca.* 5.2 after the complete photodegradation of CIP. Such a fact nicely corroborates the formation of CO_2, as the pH for the dissolved CO_2 in water is *ca.* 5.6 (*vide infra*).[16–18,52,110] The pH of the solution was regarded as a notable parameter that may have a considerable effect on the photodegradation. Thus, the effect of pH on the photodegradation of CIP was studied at 5.5, 6.0, 6.5, and 7.5 pHs. Notably, the rate of CIP photodegradation increased as a function of the pH of the solution. The maximum rate of photodegradation (k = 0.0433 min^{-1}) was observed at pH 7.5 (Fig. 4b–d and Table S4, SI). However, at lower pH (pH = 5.5; k = 0.0132 min^{-1}), CIP was only 41% degraded (Fig. S22, SI). Various ROS, such as $^{\bullet}OH$ and $^{\bullet}O_2^-$, are known to be sensitive to the pH of the reaction medium, while a basic pH favours their formation (*vide infra*).[13,111,112] As a result, subsequent photocatalytic reactions were carried out at pH 7.5. To substantiate the stability of Ln-MOFs at different pH values, the PXRD patterns of **1-Tb** were measured after immersing the sample in aqueous solutions of different pH values. In all cases, the PXRD patterns matched well with those of the as-synthesized sample, including the Le Bail refinement (Fig. S20 and S21, SI). This fact confirms the stability of Ln-MOFs under different pH values (5.5–7.5).

Characterization of photodegradation products

NMR spectral and gas chromatography (GC) experiments were performed to gain insight into CIP degradation, including its possible chemical changes and *in situ*-formed intermediates.[52,113–115] The NMR spectra of a reaction mixture were recorded at different reaction times (0, 40 min/half reaction time, and 80 min/complete reaction time). The ^{1}H NMR spectra of a reaction mixture after 40 min of photolysis showed that the majority of the aromatic resonances (7–9 ppm) disappeared, while peaks corresponding to the aliphatic groups were reduced in intensity and were slightly shifted, indicating a partial degradation (Fig. S23, SI). Similarly, in ^{13}C NMR spectra, the characteristic aromatic peaks (105–180 ppm) dis-

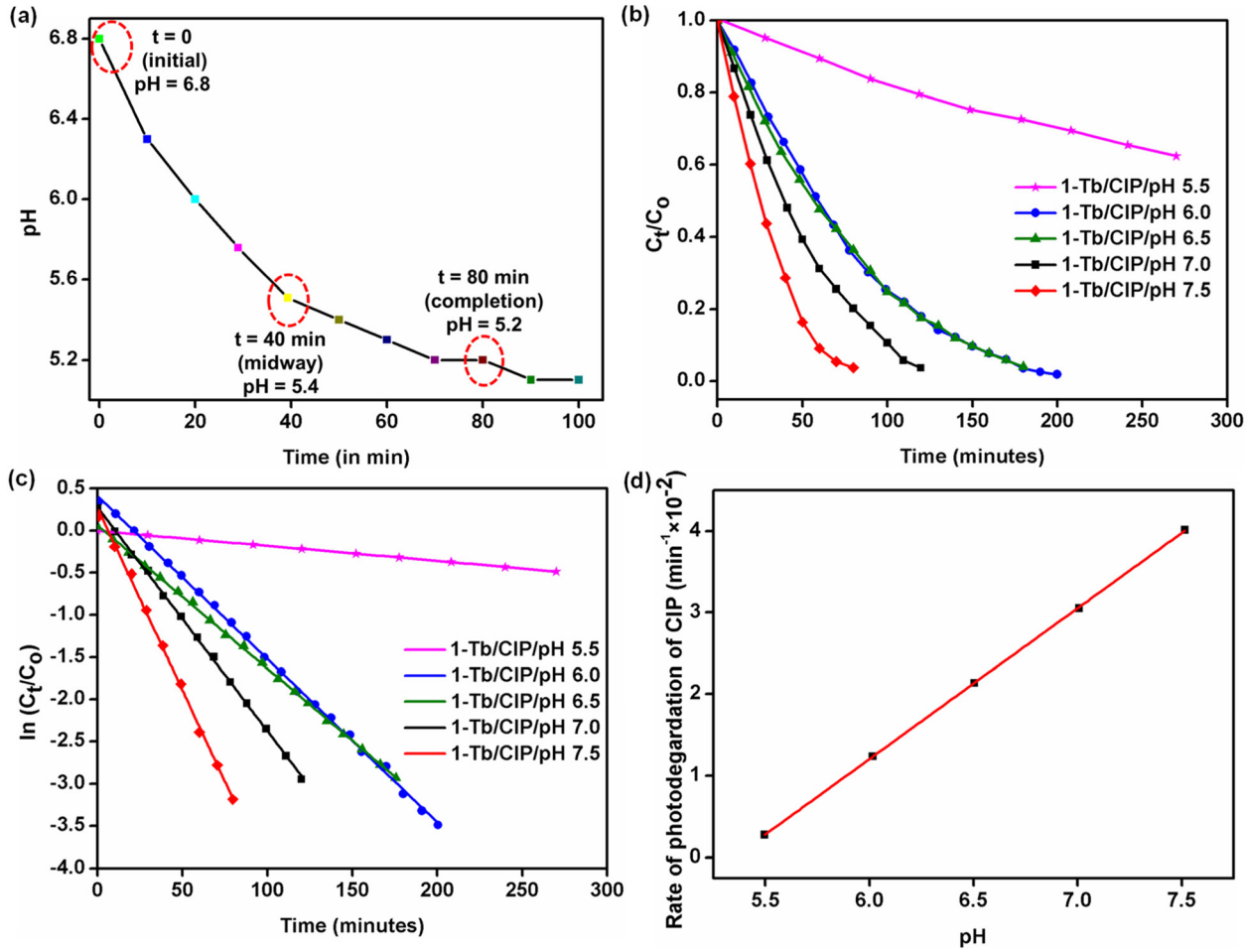

Fig. 4 (a) Plot for the variation of pH with irradiation time for the photocatalytic degradation of CIP using **1-Tb**. (b) Photocatalytic activity of **1-Tb** for the degradation of CIP at different pH values. (c) Plot of $\ln(C_t/C_0)$ *versus* time representing the first-order kinetics for the degradation of CIP using **1-Tb** at different pH values. (d) Plot for the rate of photodegradation of CIP catalyzed by **1-Tb** as a function of pH.

appeared completely, whereas new peaks, noted in the aliphatic region, are associated with the intermediates formed during the degradation (Fig. S24, SI). In fact, upfield signals, both in ^{1}H and ^{13}C NMR spectra, are most likely due to some low-molecular-weight aliphatic compounds.[113,52] In addition, the ^{13}C NMR spectrum revealed an intense peak at 124 ppm. Upon extended photolysis (*ca.* 80 min), both ^{1}H and ^{13}C NMR spectra were signal-less, suggesting a complete degradation of CIP. However, the only signal at 124 ppm intensified in the ^{13}C NMR spectrum. The said signal corresponded to the characteristic peak of CO_2 gas. To validate this, the ^{13}C NMR spectrum of a standard sample of CO_2 gas in D_2O was recorded, which matched exactly with the peak at 124 ppm (Fig. S24, SI). It is thus concluded that CO_2 was formed after the complete mineralization of CIP along with other products.[16–18,87,114,115] Subsequently, GC analysis was performed to examine the gaseous products obtained after the photodegradation of CIP. The GC signals were attributed to CO_2 (59.35%) and N_2 (4.31%) gases, revealing a close match between the calculated and the experimental values (Fig. S25, SI). Collectively, these experiments support a complete mineralization of CIP as follows:

$$2C_{17}H_{18}FN_3O_3 + 40O_2 \rightarrow 34CO_2\,(60.71\%) + 18H_2O\,(32.14\%) + 3N_2\,(5.35\%) + F_2\,(1.78\%)$$

Fluorine gas reacts with water to form HF, which is known to decolorize a distinct dark red colour of $Fe(SCN)_2$ while forming FeF_2.[116] The same reaction was noted in the present case.

$$F_2 + H_2O \rightarrow HF + O_2$$

$$\underset{\text{(red colour)}}{Fe(SCN)_2} + 2F^- \rightarrow \underset{\text{(colourless)}}{FeF_2} + 2SCN^-$$

Photophysical properties of the metalloligand and Ln-MOFs

The photocatalytic results revealed that while Ln-MOFs (**1-Tb**/**1-Eu**) are active for the photodegradation of CIP, metalloligand **1** was completely inactive. To understand the reason behind such a stark difference, photoluminescence (PL), electro-

chemical impedance spectroscopy (EIS), and transient absorption spectroscopy (TAS) studies were conducted.[117–121] The PL intensity of a semiconductor can be used to correlate the recombination rate of the photogenerated charge carriers.[117] Metalloligand **1** exhibited a strong emission band, suggesting a large recombination rate of the photogenerated electron–hole pairs. Such a situation significantly suppresses the photocatalytic activity.[117] Importantly, both **1-Tb** and **1-Eu** showed a much lower PL intensity when compared to **1**. This fact is indicative of a decrease in the recombination rate of the photogenerated electron–hole pairs, which significantly enhances the photocatalytic activity.[117] Among the two materials, **1-Tb** showed much lower PL intensity, thus advocating the lower recombination rate of charge carriers and superior photocatalytic performance (Fig. 5a). Such a fact correlates very well with the observed rate constant for the degradation of CIP.

Another important factor that significantly influences photocatalytic activity is the interfacial charge separation and the migration efficiency.[118] Thus, EIS studies were conducted to examine the interfacial charge separation property of metalloligand **1** and its Ln-MOFs, **1-Tb** and **1-Eu**. The arc radius in the Nyquist plot represents the interface layer resistance at the electrode surface; a narrower arc implies lower resistance and more effective separation of the photogenerated electron–hole pairs.[118] A much smaller arc radius for **1-Tb**, in comparison with **1**, indicates a higher efficiency of the photoinduced charge transfer, *i.e.*, a large spatial separation between the photo-electrons and holes (e_{CB}^- + h_{VB}^+). Such a fact largely suppresses the charge carrier recombination and improves their participation in the photocatalytic reaction. On the other hand, the arc radius of **1-Eu** was comparatively larger than that of **1-Tb**, suggesting a lower separation between the charge carriers and thus lower photocatalytic performance (Fig. 5b). In consensus, metalloligand **1** exhibits a much larger arc radius, thus fully justifying its ineffectiveness as a photocatalyst.

Finally, TAS studies were conducted to examine the dynamics of charge carriers in metalloligand **1** and Ln-MOFs.[119–121] Upon 400 nm excitation, both **1** and Ln-MOFs depicted broad positive absorption bands ($\Delta A > 0$) in the range of 450–800 nm (Fig. 5c–e). To understand the decay process, the kinetics of the photoinduced charges were probed at 530 nm for **1**, 530 nm for **1-Tb**, and 550 nm for **1-Eu**. The kinetics for both **1-Tb** and **1-Eu** followed a similar trend and were fitted using a single exponential function. In contrast, **1**, depicting a comparatively faster decay, was fitted with a bi-exponential function. The decay profiles are shown in Fig. 5f, while the fitting components are provided in Table S5 (SI).

The initial kinetic trace for the metalloligand **1** showed an ultrafast decay with τ_1 = 2.58 ps, indicating an instantaneous recombination of the charge carriers. The rapid kinetic decay was followed by a slow decay with a time scale of 40.30 ps, resulting in a τ_{av} of 30.49 ps. In comparison with metalloligand **1**, **1-Tb** demonstrated rather slower decay kinetics with τ = 60.53 ps. On the other hand, **1-Eu** showed an excited state decay of 40.37 ps (Fig. 5g). The decay kinetics for both Ln-MOFs, which are in the ps (10^{-12}) range, are consistent with the time scale for energy transfer (10^{-14}–10^{-11} s). Thus, it can be interpreted that only energy transfer occurs upon the association of Ln^{3+} ions with the metalloligands, rather than electron transfer, for which the time scale lies in the range of 10^{-9}–10^{-8} s.[119–121] This conclusion is further supported by the fact that both the metalloligand and Ln-MOFs share the same oxidation state of the Co ion (+3), as confirmed by XPS analysis (Fig. S11–S13, SI). A longer lifetime of the charge carriers in Ln-MOFs compared to that of the metalloligand confirms a reduced recombination rate of the photoexcited electrons and holes, thereby enhancing the photocatalytic activity. The slow decay kinetics in Ln-MOFs are assigned to an improved charge distribution at the interface of **1** and Ln^{3+} ions. The kinetics for two Ln-MOFs revealed **1-Tb** (60.53 ps) to be a much superior photocatalyst in comparison with its counterpart **1-Eu** (40.37 ps) and particularly metalloligand **1** (30.49 ps). In essence, active charges in **1-Tb** exhibited a nearly 2-fold longer lifetime compared to that of its building block **1**, thus justifying its remarkable photocatalytic activity for the photodegradation of antibiotics.

Collectively, these studies explain an acceleration in the electron–hole separation rate after the coordination of Ln^{3+} ions to a metalloligand **1**. This fact is responsible for the enhanced photocatalytic activity of Ln-MOFs in comparison with that of metalloligand **1**. In addition, a higher E_{HOMO}–E_{LUMO} gap, a higher PL intensity, a longer arc radius in the Nyquist plot, and a faster decay in **1-Eu**, in comparison with those of **1-Tb**, account for the former's poor photocatalytic performance for the degradation of the antibiotic, CIP.

Photocatalytic degradation of other antibiotics

The photodegradation of the remaining antibiotics was investigated using **1-Tb** and the rates (min^{-1}) varied in the following order: NOR (97%; 0.0359) > NFZ (95%; 0.0226) > FUR (93%; 0.0154) > NFT (95%; 0.0618) > TC (67%; 0.0056; TC resulted in *ca.* 91% degradation in 4 h) > PG (12%; 0.0015) > AMX (9%; 0.0009) > SQX (4%; 0.0001) (Fig. S26–S29 and Table S6, SI).

According to the conventional protocol of semiconductor photocatalysis, for successful electron transfer, the LUMO of a catalyst must be lower than the LUMO of a substrate, while the HOMO of a substrate must lie between the HOMO of a catalyst and the oxidation reaction potential.[122] Validating this principle, antibiotics with band gaps more than that of **1-Tb** [$E_{g(Antibiotic)} > E_{g(\mathbf{1\text{-}Tb})}$ (2.42 eV)] should be photodegraded (*e.g.*, CIP, NOR, NFZ, FUR, NFT and TC) while antibiotics having band gaps less than or equal to the band gap of **1-Tb** [$E_{g(Antibiotic)} \leq E_{g(\mathbf{1\text{-}Tb})}$ (2.42 eV)] should not be mineralized (*e.g.*, SQX, E_g = 2.38 eV). Due to the exceptionally high band gaps of PG (E_g = 3.51 eV) and AMX (E_g = 4.20 eV), in comparison with that of **1-Tb** (2.42 eV), photodegradation of these two antibiotics was not feasible (Fig. S30–S32, SI). Not surprisingly, these two antibiotics were photodegraded to a minimal extent.

Larger energy separation between the respective LUMO of a catalyst and an antibiotic will favour the photocatalytic process and therefore the order of photodegradation must have been: CIP (E_g = 3.17 eV) > NOR (E_g = 3.12 eV) > **NFT** (E_g = 2.60 eV) >

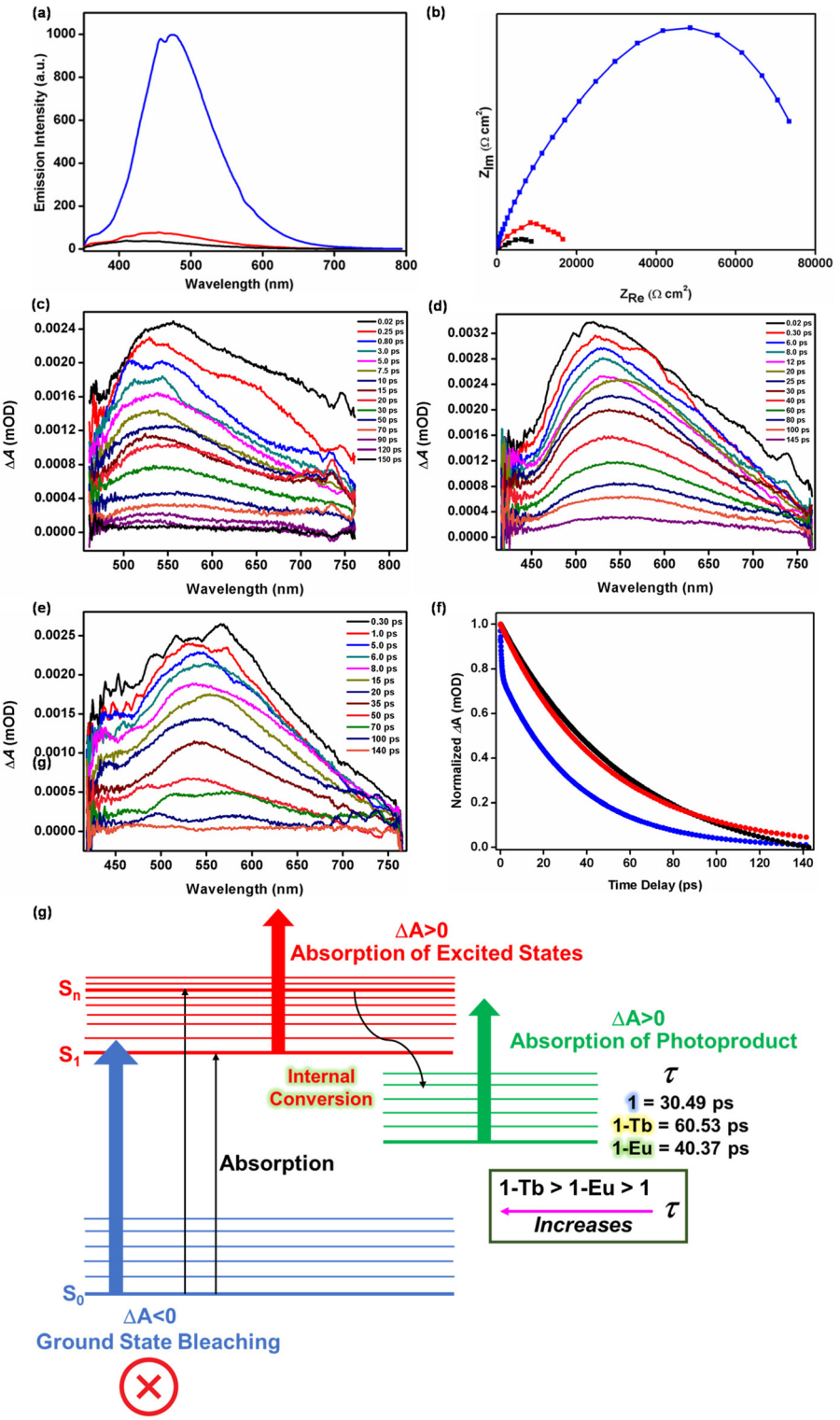

Fig. 5 (a) Photoluminescence and (b) EIS spectra of metalloligand **1** (blue trace), **1-Tb** (black trace), and **1-Eu** (red trace); λ_{ex} = 400 nm. Transient absorption spectra for (c) metalloligand **1** and Ln-MOFs, (d) **1-Tb** and (e) **1-Eu** at various time delays. (f) Corresponding kinetic traces for metalloligand **1** (blue trace), **1-Tb** (black trace), and **1-Eu** (red trace). (g) Schematic illustration of light-induced dynamics for metalloligand **1** and Ln-MOFs.

FUR (E_g = 2.53 eV) > **TC** (E_g = 2.50 eV) > **NFZ** (E_g = 2.48 eV). Importantly, however, the order of photodegradation of antibiotics presented a different order (Scheme 2). The notable difference in the photodegradation rates of different antibiotics is explained by considering the inclusion of an antibiotic molecule within the pores of a Ln-MOF and various

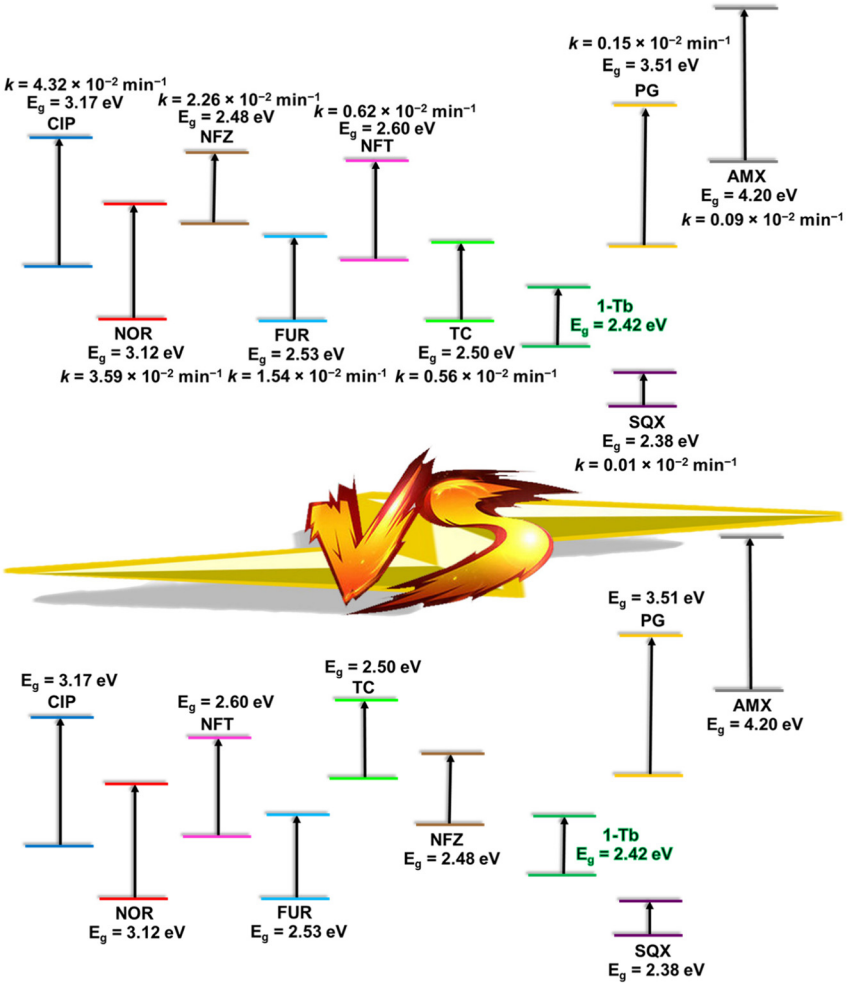

Scheme 2 A comparative illustration of the photocatalytic activity of **1-Tb** for the degradation of different antibiotics under visible-light irradiation on the basis of the HOMO–LUMO energy gaps and the rates of degradation of the respective antibiotics: observed (above) and anticipated results (below).

H-bonding interactions involved in facilitating its encapsulation (*vide infra*).

Role of H-bonding in the photocatalytic degradation of antibiotics

To gain insight into the differences in the photodegradation of various antibiotics, molecular docking studies were performed to understand the role of antibiotic encapsulation and the various non-covalent interactions that occur within the pores of Ln-MOFs.[52] In molecular docking, a molecule of CIP was found to occupy the pores of **1-Tb** while being engaged in various H-bonding interactions (Fig. 6a, b and Table S7, SI). For example, the F-atom of CIP was found to form an H-bond with the H-atom of the biphenyl ring. Similarly, CIP also interacted *via* its COO–H and N–H groups with a lattice water molecule and a free carboxylate-O group. Furthermore, CIP also interacted with the arene groups of **1-Tb** *via* C═O...H_{arene} and N...H_{arene} synthons. The arene ring of CIP was also involved in π···π stacking with the biphenyl rings (centroid-to-centroid: 3.62 Å). Such H-bonding and other interactions of CIP within the pores of the MOF allowed its effective encapsulation and potentially favoured its efficient photocatalytic degradation. Such a situation explains the rapid degradation of CIP by **1-Tb**.

To confirm the encapsulation of CIP, the FTIR spectrum of **1-Tb** impregnated with CIP was compared to that of a pristine sample of **1-Tb**. The O–H stretches of **1-Tb** were significantly red-shifted ($\Delta\nu$ = 124 cm^{-1}) from 3316 to 3192 cm^{-1}, thus, illustrating the pivotal role played by the lattice water molecules in forming H-bonds to CIP.[123] Furthermore, considerably red-shifted ($\Delta\nu$ = 125 cm^{-1}) C–H stretches of CIP were observed at 2839–2912 cm^{-1} (Fig. 6c).[124,125] These facts confirm that a molecule of CIP not only occupied the pores but also interacted with various functional groups offered by **1-Tb**.

To gain further insight into how H-bonding interactions affect photocatalytic activity, a series of control experiments was conducted. As CIP was involved in H-bonding interactions with the lattice water molecules of Ln–CP, its deuterium analogue, **1-Tb-D**, was prepared, which showed a broad peak at *ca.*

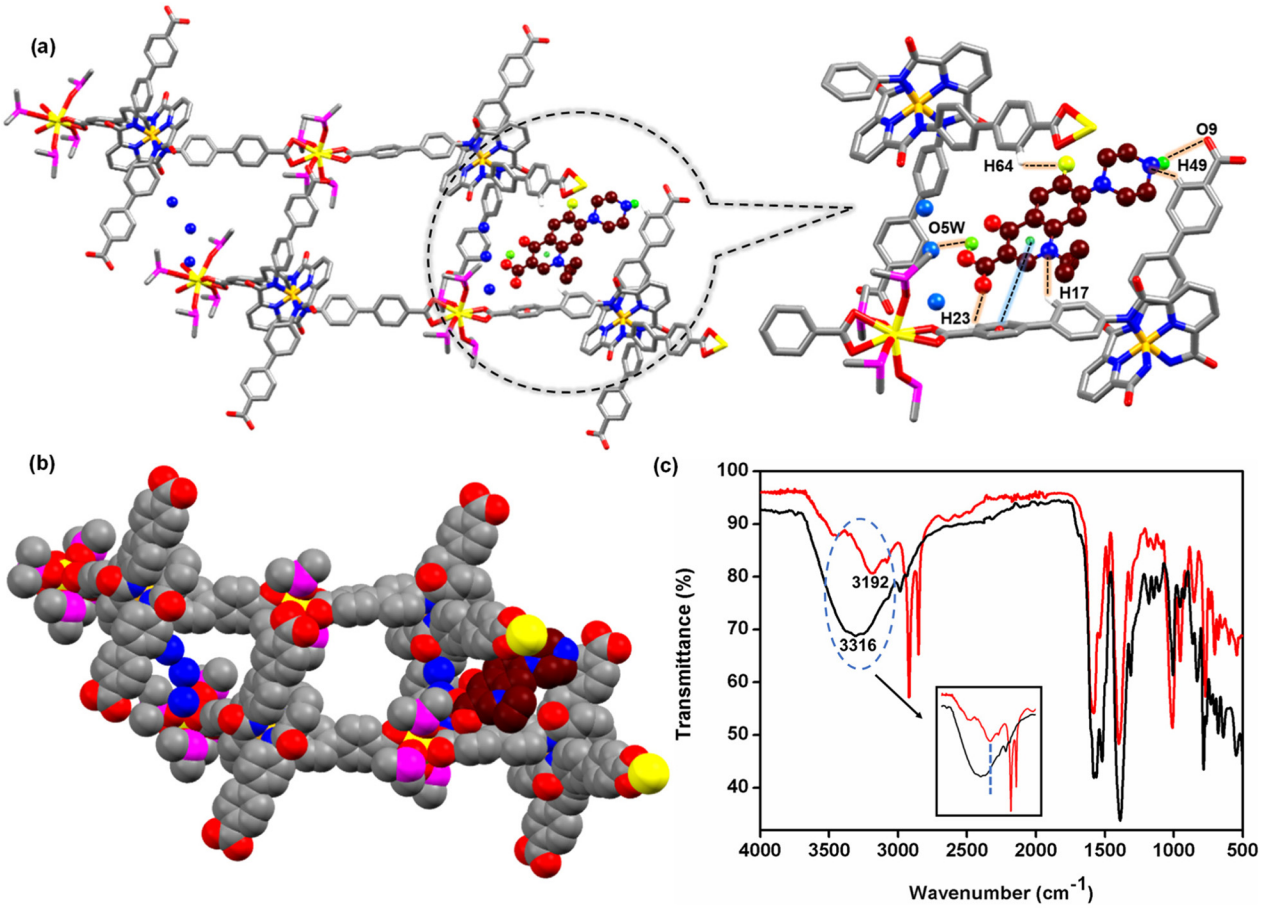

Fig. 6 (a) Molecular docking structure of **1-Tb** with CIP, where **1-Tb** is shown as a capped-stick model (color code: orange, Co; yellow, Tb; pink, S; blue, N; red, O; grey, C; and white, H), while the CIP molecule is depicted in a ball-and-stick model (color code: olive, F; blue, N; red, O; wine, C; and green, H). H atoms, except for those involved in interactions, have been omitted for clarity. π···π-stacking interactions are shown by the blue dots, whereas H-bonding interactions are presented by the red dots. (b) Molecular docking structure in a space-filling mode for **1-Tb** with CIP (wine color). (c) FTIR spectra of as-synthesised **1-Tb** (black trace) and the impregnated sample of **1-Tb** with CIP (red trace).

2478 cm^{-1} due to the O–D groups of the lattice water molecules (Fig. S33a, SI).[126]

Notably, the photodegradation of CIP by **1-Tb-D** showed a noteworthy decline to 46% (0.0042 min^{-1}) (Scheme 3a, d and Fig. S33b, S39c, SI). In line with this, the FTIR spectrum of **1-Tb-D** impregnated with CIP did not reveal significant differences compared to the as-synthesized sample of **1-Tb-D**, suggesting negligible or no binding of CIP (Fig. S33c, SI). A noteworthy decline in the rate of photodegradation supports the critical role played by the H-bonding interactions between a CIP molecule and Ln–CP in promoting the photocatalysis. Very similarly, photodegradation of the deuterated analogue of CIP (D-CIP) with **1-Tb** revealed a slower rate (0.0078 min^{-1}) with only 35% degradation (Scheme 3d and Fig. S33d, e, S39c, SI). As expected, photodegradation of D-CIP employing **1-Tb-D**, as a photocatalyst, showed the slowest rate of the reaction with a 71% decline (0.0024 min^{-1}) (Scheme 3d and Fig. S33f, S39c, SI). Collectively, these experiments provide convincing support for the role of H-bonding in substrate binding and subsequent photocatalysis.[105–107]

In the next step, CIP was subjected to a few structural modifications to selectively alter the functional groups involved in H-bonding interactions. For example, methylation of the N–H group of the piperazinyl ring resulted in CH_3-N-CIP while esterification of the COO–H group produced CH_3COO-CIP (Fig. S34–S37, SI).[127,128] The substitutions of the said functional groups, which were involved in H-bonding interactions between CIP and **1-Tb**, are likely to alleviate such interactions and consequently affect the photodegradation efficiency (Fig. S38 and Table S7, SI). As expected, the use of both CH_3-N-CIP (10% decline; 0.0164 min^{-1}) and CH_3COO-CIP (35% decline; 0.0072 min^{-1}) considerably reduced their rate of degradation (Schemes 3b–d and Fig. S39, SI). In essence, the rate of photodegradation varies as follows: CIP (0.0265 min^{-1}) > CH_3-N-CIP (0.0164 min^{-1}) > D-CIP (0.0078 min^{-1}) > CH_3COO-CIP (0.0072 min^{-1}) > **1-Tb-D**/CIP (0.0042 min^{-1}) > **1-Tb-D**/D-CIP (0.0024 min^{-1}) (Table S8, SI). These experiments not only confirm the potential sites of H-bonding interactions between a drug molecule and photocatalyst but also provide substantial evidence about their key roles in controlling the photodegradation efficiency.

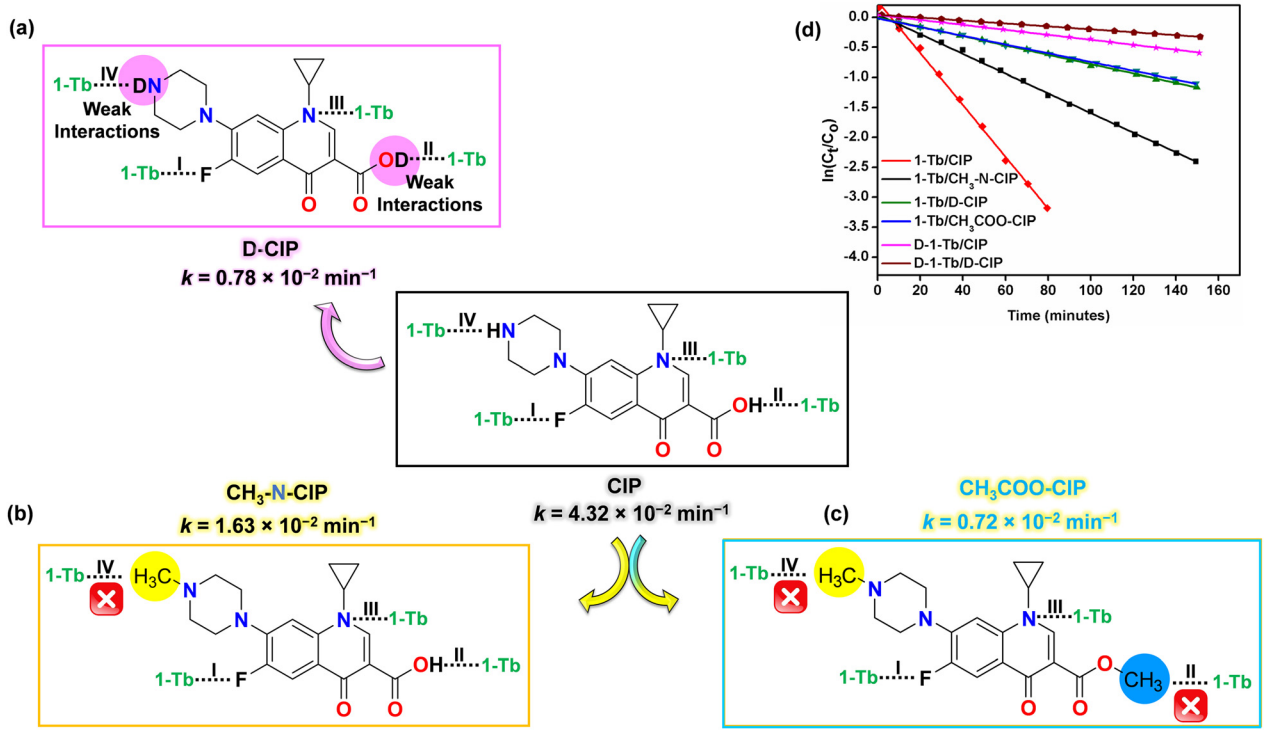

Scheme 3 Schematic illustrations of the photocatalytic degradation of CIP, using **1-Tb**, under different conditions: (a) D-CIP, (b) CH_3-N-CIP, and (c) CH_3COO-CIP. Black dots represent H-bonding interactions between CIP and **1-Tb** *via* (I) an F atom; (II) a COO-H atom; (III) an N (quinolone ring) atom, and (IV) an N–H (piperazinyl ring) atom (for details, see the text). (d) Plots of $\ln(C_t/C_0)$ *versus* time representing the first-order kinetics for the degradation of CIP under different conditions using **1-Tb**. The photodegradation of CIP was studied in each case for 150 minutes in order to evaluate the kinetics, although, in each case, complete degradation was accomplished in *ca.* 4 hours.

The molecular docking of other antibiotics (FUR, NFT, NOR, NFZ, and TC) with **1-Tb** revealed strong H-bonding interactions wherein all antibiotics, except TC, were fully encapsulated within the pores of **1-Tb** (Fig. S40–S42 and Table S7, SI). This fact adequately justifies the slow photodegradation of TC in comparison with that of other antibiotics. However, the molecular docking studies of antibiotics PG, AMX, and SQX are not included as these antibiotics could not be degraded using **1-Tb** (*vide supra*).

These findings convincingly explain the disparity between the observed and anticipated trends of the photodegradation of various antibiotics. The primary factor responsible for the photodegradation was, undisputedly, the ability of a semiconductor Ln–CP to support visible-light absorption and the synchronicity between the HOMO–LUMO gap of Ln–CP and an antibiotic. However, at the same time, the photodegradation rate was also controlled by the type and strength of various interactions that existed between a drug molecule and the photocatalyst.[52] Any antibiotic that was bound effectively within the cavity of Ln–CP and displayed stronger interactions exhibited a higher rate of photodegradation in comparison with those that exhibited poor fitting and thus weaker interactions.

Several reports on the utilization of metal oxides, composites, *etc.*, for the degradation of antibiotics are available in the literature; however, the majority of these examples have primarily focused on the photocatalytic degradation of only select antibiotics, such as TC.[16–18,87,129–133] In fact, TC is known to self-photolyze (k = 0.0003–0.0011 min^{-1} in the pH range of 6.0–9.0) under the simulated sunlight owing to its ability to generate ROS (primarily $^1O_2$).[134] The presence of a semiconductor-based photocatalyst is assumed to just facilitate TC degradation rather than significantly catalyzing it. Unlike the reported materials, the present Ln-MOFs have illustrated their ability to completely photodegrade a wide range of antibiotics from different chemical classes. The photodegradation efficiency of the present Ln-MOFs towards assorted antibiotics is superior to that of other MOFs, MOF-based composites, and heterojunctions (Table S4, SI; comparative analysis for the degradation of only CIP is illustrated).[24,129–133] Additionally, unlike in the present case, the reported materials have often employed photodegradation reactions using an external oxidant, such as H_2O_2.[16–18,24,129–133] Thus, the present photocatalysts are noteworthy.

Generation of ROS and scavenger studies

In a typical photocatalysis, a semiconductor material, upon light irradiation (with the energy of the excitation source higher than the band gap of the material), results in photon absorption, causing the excitation of an electron (e^-) from the HOMO to LUMO while leaving a hole (h^+) in the HOMO.[1–15] The photo-electrons (e^-) and holes (h^+) are strong reductants

and oxidants, respectively. Such species can migrate to the surface of the photocatalyst and rapidly react with the surface-adsorbed molecules and/or ions to form the reactive radical species (ROS). The hydroxyl radical ($^{\bullet}OH$), one of the most powerful but nonselective oxidizing radicals, can be formed by the oxidation of both OH^- and surface-adsorbed water molecules by h^+ (eqn (1) and (2)).[13–15]

$$OH^- + h_{HOMO}{}^+ \rightarrow {}^{\bullet}OH \quad [E^{\circ}({}^{\bullet}OH/OH^-) = 1.89\ V] \qquad (1)$$

$$H_2O + h_{HOMO}{}^+ \rightarrow {}^{\bullet}OH + H^+ \quad [E^{\circ}({}^{\bullet}OH/H_2O) = 2.65\ V] \qquad (2)$$

The O_2 molecule can trap the photo-electron to form a superoxide radical ($^{\bullet}O_2^-$), which is a mild oxidant (eqn (3)). A superoxide radical can combine with a hole (h^+) to produce singlet oxygen ($^1O_2$, eqn (4)).[13–15]

$$O_2 + e_{LUMO}{}^- \rightarrow {}^{\bullet}O_2{}^- \quad [E^{\circ}(O_2/{}^{\bullet}O_2{}^-) = -0.33\ V] \qquad (3)$$

$${}^{\bullet}O_2{}^- + h_{HOMO}{}^+ \rightarrow {}^1O_2 \qquad (4)$$

Eventually, such ROS ($^{\bullet}OH$, $^{\bullet}O_2^-$ and $^1O_2$), produced by a series of photocatalytic reactions, could lead to the chemical breakdown of a drug molecule into simpler products.[1–18]

In order to ascertain whether the present Ln-MOFs support free radical-based reactions, activation energy (E_a) was calculated. Typically, heterolytic reactions exhibit high values of E_a, whereas low E_a signifies free-radical-based reactions.[135,136] Thus, photocatalytic reactions were performed at different temperatures (°C): 10, 20, 25, 30, and 40 to determine the E_a for the degradation of CIP (Fig. S48, SI). E_a, as calculated using the Arrhenius equation, was found to be 23.89 kJ mol^{-1} (Fig. 7a). A relatively smaller value of E_a suggests that the photodegradation of CIP is likely to be a free radical-based reaction.[136,52a]

To support such a fact and to prove the involvement of various ROS, a few radical quenchers were employed during the photodegradation of CIP.[13–15] Notably, the use of benzoquinone (BQ; 27%; 0.0023 min^{-1}) and isopropyl alcohol (IPA; 56%; 0.0046 min^{-1}) significantly slowed the degradation of CIP, thus emphasizing the role of $^{\bullet}O_2^-$ and $^{\bullet}OH$, respectively (Fig. 7b, c and Fig. S49a, b, SI). However, the use of NaN_3 (64%, 0.0064 min^{-1}) and $(Na)_2EDTA$ (65%, 0.0081 min^{-1}) as the scavengers for $^1O_2$ and h^+, respectively, led to a modest drop in the degradation activity (Fig. 7b, c and Fig. S49c, d, SI). Collectively, these experiments imply that while $^{\bullet}OH$ and $^{\bullet}O_2^-$ are the major ROS, both h^+ and $^1O_2$ are not the significant species for the photodegradation of CIP (Fig. 7d and Fig. S50, SI).

Subsequently, the concentrations of the dominant ROS, $^{\bullet}OH$ and $^{\bullet}O_2^-$, were estimated quantitatively. Coumarin is known to selectively react with $^{\bullet}OH$ to produce an emissive 7-hydroxycoumarin.[13] By monitoring a gradual increase in the emission intensity at 448 nm, for the generation of 7-hydroxycoumarin, under the visible light irradiation in the case of **1-Tb**, the concentration of hydroxyl radicals was calculated to be

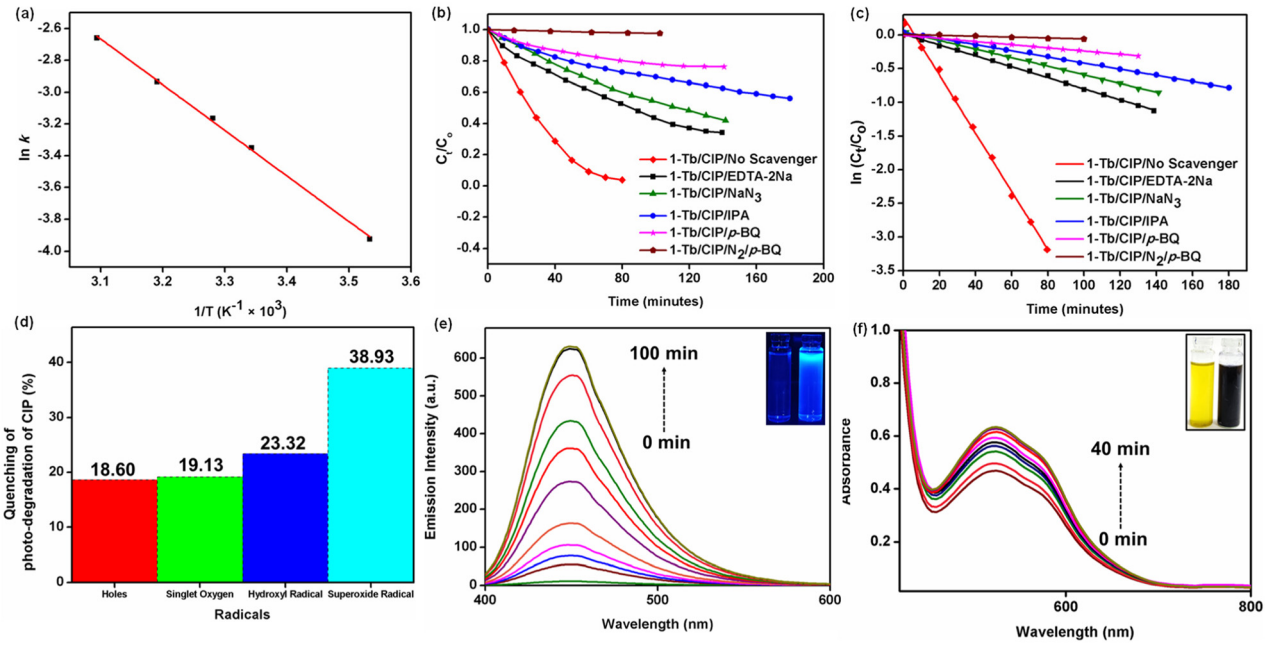

Fig. 7 (a) Arrhenius plot of ln(k) *versus* 1/T. (b) Photocatalytic activity of **1-Tb** for the degradation of CIP in the presence of different scavengers. (c) Plot of ln(C_t/C_0) *versus* time representing the first-order kinetics for the degradation of CIP with **1-Tb** in the presence of different scavengers. (d) Contribution of ROS in the reduction of the photoactivity of **1-Tb** for the photodegradation of CIP. (e) Emission spectrum for the generation of 7-hydroxycoumarin from coumarin during a photocatalysis experiment in the presence of **1-Tb** under visible-light irradiation at different times (0–100 min at an interval of 10 min) (inset: digital photographs of a coumarin solution at different times). (f) Absorption spectrum for the production of NBT-MF during a photocatalysis experiment of NBT in the presence of **1-Tb** under visible-light irradiation at different times (0–40 min at an interval of 5 min) (inset: digital photographs of **1-Tb** + NBT solution at different times).

3.15 μM (Fig. 7e). Similarly, the nitro blue tetrazolium (NBT) assay was used to confirm the concentration of $^{\bullet}O_2^-$ radicals.[13] Depending on the O_2 saturation level, NBT preferentially reacts with $^{\bullet}O_2^-$ to form purple coloured monoformazan and diformazan. When a DMSO solution containing **1-Tb** and NBT was exposed to visible light, a peak at 530 nm, corresponding to monoformazan, was observed. Time-dependent monitoring enabled the calculation of the concentration of the superoxide radicals to be 5.28 μM (Fig. 7f). These results correlate well with the rate constants for the degradation of CIP in the presence of the respective scavengers.

Mechanistic insights

The generation of various ROS is driven by the redox potentials of the species involved. To investigate whether the present Ln-MOFs favour the formation of ROS ($^{\bullet}OH$ and $^{\bullet}O_2^-$), their band gap structures need to be critically analyzed (Scheme 4). The generation of superoxide radicals ($^{\bullet}O_2^-$) is energetically viable since the LUMO potential for both **1-Tb** and **1-Eu** is more negative than that of the $O_2/^{\bullet}O_2^-$ couple. The HOMO potential, however, is considerably less favourable to cause oxidation of hydroxide ions or surface water molecules to produce the hydroxyl radicals (eqn (5)). The ROS scavenger experiments, however, suggested otherwise (eqn (5), *vide infra*). Therefore, it became essential to identify the source of hydroxyl radicals ($^{\bullet}OH$).

$$OH^- + h_{HOMO}{}^+ \rightarrow {}^{\bullet}OH \ [\textbf{Not feasible}] \quad (5)$$

In fact, hydroxyl radicals can also be generated by a chain of reactions wherein a superoxide radical first combines with protons and electrons to form H_2O_2 (eqn (6)), which is then reduced by an electron to form $^{\bullet}OH$ (eqn (7)).[112]

$$^{\bullet}O_2^- + 2H^+ + 2e^- \rightarrow H_2O_2 \quad [E^{\circ}(^{\bullet}O_2^-/H_2O_2) = 1.73\ V] \quad (6)$$

$$H_2O_2 + e^- \rightarrow {}^{\bullet}OH + OH^- \quad [E^{\circ}(H_2O_2/{}^{\bullet}OH) = 0.88\ V] \quad (7)$$

In order to confirm the generation of hydroxyl radicals *via* this pathway, CIP degradation was carried out under a N_2 atmosphere to eliminate the generation of superoxide radicals from dissolved O_2. Furthermore, the addition of *p*-BQ to such a reaction mixture largely prevented the generation of any $^{\bullet}O_2^-$. Consequently, CIP degradation declined from 98% under air-equilibrated conditions to *ca.* 10% under a N_2 environment (k = 0.0006 min^{-1}) (Fig. 7b, c and Fig. S49e, SI). This experiment validated the significance of $^{\bullet}O_2^-$ for the generation of $^{\bullet}OH$.[13–18] Energetically as well, both **1-Tb** and **1-Eu** favoured the formation of $^{\bullet}OH$ *via* this pathway.[13–15] These studies thus confirm that holes cannot initiate the formation of hydroxyl radicals, which mainly originate from $^{\bullet}O_2^-$.

To further confirm the generation of ROS, electron paramagnetic resonance (EPR) spectra were recorded. A blank line under darkness indicates that the generation of free radicals is a light-mediated process. On visible light irradiation of an aqueous solution containing **1-Tb**, a sharp EPR signal was detected at g = 2.00, characteristic of a free-radical species ($^{\bullet}O_2^-/{}^{\bullet}OH$), whose intensity increased significantly with an increase in the photo-irradiation (Fig. S49f, SI).[13–15]

As previously discussed, the pH of the reaction medium significantly influences the photodegradation of CIP, favouring its decay at neutral to alkaline pH while inhibiting it at acidic pH. It is well-acknowledged that the formation of ROS is also pH-dependent.[3,15,18] At low pH, $^{\bullet}O_2^-$ exists in its protonated form, perhydroxyl radical ($HO_2^{\bullet}$), with a pK_a ($HO_2^{\bullet}/{}^{\bullet}O_2^-$) of 4.8 (eqn (8)).[137–139] The formation of $HO_2^{\bullet}$ was encouraged by a favourable redox potential for both **1-Tb** and **1-Eu**. The anion radical $^{\bullet}O_2^-$, having a reducing property, is known to be less reactive compared to $HO_2^{\bullet}$, which exhibits an oxidizing property even at low concentration at the physiological pH. The

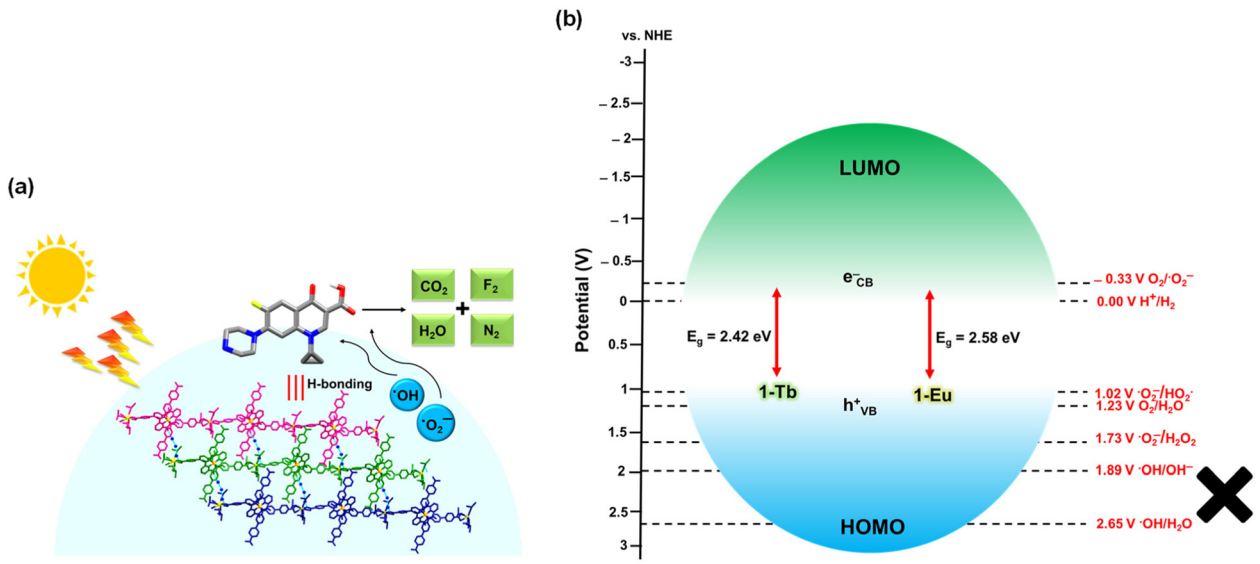

Scheme 4 (a) Schematic illustration depicting various steps for the degradation of antibiotics by Ln-MOFs under visible-light irradiation. (b) Redox potentials of common reactive species in photocatalysis.

reactive $HO_2^{\bullet}$ can combine with protons to form $^{\bullet}OH$ (eqn (9)). At pK_a 11.9, $^{\bullet}OH$ converts to its conjugate base $^{\bullet}O-$.[137–139] The oxide radical ($^{\bullet}O-$) is comparatively less reactive, thus accounting for a decreased photodegradation of CIP at acidic pH. This is not relevant at physiological pH, justifying a higher rate of CIP degradation at pH 7. In contrast, a basic reaction medium promotes the overall reaction, resulting in the formation of $^{\bullet}OH$, justifying the highest rate of degradation at pH 7.5.

$$^{\bullet}O_2^- + H^+ \rightarrow HO_2^{\bullet} \quad [E^{\circ}(^{\bullet}O_2^-/HO_2^{\bullet}) = 1.02\ V] \qquad (8)$$

$$2HO_2^{\bullet} + 2H^+ \rightarrow H_2O_2 + 2\ ^{\bullet}OH \qquad (9)$$

Control and reusability experiments

The visible-light-driven photocatalysis of the present heterogeneous Ln-MOFs is of great importance for practical applications. Thus, the recyclability and reusability of Ln-MOFs were studied, taking **1-Tb** as a representative case. After the photodegradation experiment, **1-Tb** was isolated by centrifugation and subjected to the successive cycles of photocatalysis. Even after five repetitive cycles, the photocatalyst **1-Tb** maintained its effectiveness, showing up to 95% degradation efficiency (Fig. S43, SI). Moreover, both stability and robustness of Ln-MOFs were verified by FTIR spectral and PXRD studies (Fig. S44–S46, SI). Both these studies asserted that both Ln-MOFs remained stable after the photodegradation cycles. Furthermore, optical and SEM images of the recovered samples exhibited no major changes in their morphology, thus again suggesting a robust nature of Ln-MOFs (Fig. 3f, g and Fig. S47, SI). It is thus clear that both Ln-MOFs can be employed as promising heterogeneous photocatalysts for the treatment of wastewater due to their high stability and excellent photocatalytic efficiency.

Conclusions

This work has described the design and synthesis of two Ln-MOFs based on an Earth-abundant metal-based light-harvesting metalloligand. Due to the encouraging photoactive merits of Ln-MOFs, they were used as robust heterogeneous photocatalysts for the degradation of selected antibiotics. Both Ln-MOFs were capable of efficiently photodegrading a variety of antibiotics belonging to different chemical classes. The photodegradation mechanism was systematically studied with the aid of transient absorption spectroscopy, photoluminescence, electrochemical, and radical scavenging studies. Along with excellent photophysical properties, both materials presented unique H-bonding characteristics, which significantly enhanced their photodegradation performance. The noteworthy synchronicity between photodegradation activities and H-bonding-based substrate encapsulation is unprecedented and has not been paid sufficient attention in the past. The present results open up new opportunities for the development of light-harvesting metalloligand-based photocatalysts that also incorporate significant features of MOFs into the material design. It is expected that such a strategy will help in the design of next-generation highly efficient photocatalysts.[140]

Author contributions

RuG designed the research work, conducted experiments, analysed data, and drafted the first draft of the manuscript. SM and PKC contributed to the TAS experiments, assisting with both experiments and data analysis. RG conceived the idea, coordinated research, acquired funds, and contributed to the review and drafting of the final manuscript. All authors read and approved the final version of the manuscript.

Conflicts of interest

There are no conflits to declare.

Data availability

The necessary data pertaining to this article are available in the supplementary information (SI). Supplementary information is available. See DOI: **https://doi.org/10.1039/d5qi01850a**.

CCDC 2485439 and 2485440 contain the supplementary crystallographic data for this paper.[141a,b]

Acknowledgements

RG gratefully acknowledges financial support from the Science & Engineering Research Board (SERB), New Delhi (CRG/2021/001700). RuG thanks CSIR, New Delhi, for her SRF fellowship. The authors thank USIC at this university for the instrumental facilities and Dr Gulshan Kumar for the synthesis of ligands and metalloligands. P.K.C. thanks DST-FIST (SR/FST/CS-II-027/2014) for providing funds for the ultrafast TA facility. S.M. thanks MHRD (GoI) for the Prime Minister's Research Fellowship (PMRF ID: 1401240).

References

1 S. Zhu and D. Wang, Photocatalysis: Basic Principles, Diverse Forms of Implementations and Emerging Scientific Opportunities, *Adv. Energy Mater.*, 2017, **7**, 1700841.
2 M. Melchionna and P. Fornasiero, Updates on the Roadmap for Photocatalysis, *ACS Catal.*, 2020, **10**, 5493–5501.
3 M. Fang, X. Tan, Z. Liu, B. Hu and X. Wang, Recent Progress on Metal-Enhanced Photocatalysis, A Review on the Mechanism, *Research*, 2021, 794329.
4 A. Ismail and D. W. Bahnemann, Photochemical Splitting of Water for Hydrogen Production by Photocatalysis: A Review, *Sol. Energy Mater. Sol. Cells*, 2014, **128**, 85–101.

5 X. Yang and D. Wang, Photocatalysis: From Fundamental Principles to Materials and Applications, *ACS Appl. Energy Mater.*, 2018, **1**, 6657–6693.
6 R. B. P. Marcelino and C. C. Amorim, Towards Visible-Light Photocatalysis for Environmental Applications: Band-Gap Engineering versus Photons Absorption—a Review, *Environ. Sci. Pollut. Res.*, 2019, **26**, 4155–4170.
7 B. Liu, X. Zhao, C. Terashima, A. Fujishima and K. Nakata, Thermodynamic and Kinetic Analysis of Heterogeneous Photocatalysis for Semiconductor Systems, *Phys. Chem. Chem. Phys.*, 2014, **16**, 8751–8760.
8 Y. Qu and X. Duan, Progress, Challenge and Perspective of Heterogeneous Photocatalysts, *Chem. Soc. Rev.*, 2013, **42**, 2568–2580.
9 A. B. Djurišić, Y. He and A. M. C. Ng, Visible-Light Photocatalysts: Prospects and Challenges, *APL Mater.*, 2020, **8**, 030903.
10 J. Low, J. Yu, M. Jaroniec, S. Wageh and A. A. Al-Ghamdi, Heterojunction Photocatalysts, *Adv. Mater.*, 2017, **29**, 1601694.
11 B. Ohtani, Photocatalysis A to Z—What We Know and What We Do Not Know in a Scientific Sense, *J. Photochem. Photobiol.*, 2010, **11**, 157–178.
12 N. Serpone and A. V. Emeline, Semiconductor Photocatalysis—Past, Present, and Future Outlook, *J. Phys. Chem. Lett.*, 2012, **3**, 673–677.
13 Y. Nosaka and A. Y. Nosaka, Generation and Detection of Reactive Oxygen Species in Photocatalysis, *Chem. Rev.*, 2017, **117**, 11302–11336.
14 L. Luo, T. Zhang, M. Wang, R. Yun and X. Xiang, Recent Advances in Heterogeneous Photo-Driven Oxidation of Organic Molecules by Reactive Oxygen Species, *ChemSusChem*, 2020, **13**, 5173–5184.
15 L. Xiong and J. Tang, Strategies and Challenges on Selectivity of Photocatalytic Oxidation of Organic Substances, *Adv. Energy Mater.*, 2021, **11**, 2003216.
16 J. J. Rueda-Marquez, I. Levchuk, P. Fernández Ibañez and M. Sillanpää, Critical Review on Application of Photocatalysis for Toxicity Reduction of Real Wastewaters, *J. Cleaner Prod.*, 2020, **258**, 120694.
17 M. T. Yagub, T. K. Sen, S. Afroze and H. M. Ang, Dye and Its Removal from Aqueous Solution by Adsorption: A Review, *Adv. Colloid Interface Sci.*, 2014, **209**, 172–184.
18 V. I. Parvulescu, F. Epron, H. Garcia and P. Granger, Recent Progress and Prospects in Catalytic Water Treatment, *Chem. Rev.*, 2022, **122**, 2981–3121.
19 B. M. Hockin, C. Li, N. Robertson and E. Zysman-Colman, Photoredox catalysts based on earth-abundant metal complexes, *Catal. Sci. Technol.*, 2019, **9**, 889–915.
20 X. Han, Z. Yin, Y. Yang, Y. Chen, Z. Hong, C. Xie, Y. Luo and M. Xue, Biomimetic lotus leaf inspired superhydrophobic BN/MWCNTs/Graphene composited membrane for enhanced thermal performance, *J. Mater. Sci.*, 2025, **60**, 15606–15623.
21 P. Sharma, M. Ahmad, N. Haq, A. A. Kumar and K. A. Siddiqui, Ultrasensitive Detection and Photodegradation of Naproxen in Water via a Cationic $[Co(BPMEDA)Cl_2]^{2+}$ Coordination Network, *ACS Appl. Opt. Mater.*, 2025, **3**, 1388–1409.
22 M. Kukreja, A. A. Kumar, N. Haq and K. A. Siddiqui, Nickel-doped cadmium coordination polymers (Ni@Cd-CP-n): A dual-function platform for antibiotic detection and dye photodegradation, *Mater. Today Commun.*, 2025, **45**, 112403.
23 G. Yang, Z. Yin, X. Han, Y. Ma, J. Xu, Z. Hong, C. Xie, Y. Luo and M. Xue, Pyramidal array Janus hydrogel-based solar evaporator via broadband light trapping inspired by durian peel for efficient seawater desalination, *Water Res.*, 2025, **287**, 124375.
24 R. K. Dharman, A. Kausalya, S. Vargheese, S. Lakshmipathi and T. H. Oh, Construction of Cu-MOF@Bi_2MoO_6 Z-scheme heterostructure mediated by Bi nanoparticles and oxygen vacancies for ciprofloxacin degradation and mechanism investigation, *Environ. Sci.: Nano*, 2025, **12**, 3488–3502.
25 J.-H. Shon and T. S. Teets, Molecular Photosensitizers in Energy Research and Catalysis: Design Principles and Recent Developments, *ACS Energy Lett.*, 2019, **4**, 558–566.
26 D. M. Schultz and T. P. Yoon, Solar Synthesis: Prospects in Visible Light Photocatalysis, *Science*, 2014, **343**, 1239176.
27 X. Yu, L. Wang and S. M. Cohen, Photocatalytic Metal–Organic Frameworks for Organic Transformations, *CrystEngComm*, 2017, **19**, 4126–4136.
28 S. Angerani and N. Winssinger, Visible Light Photoredox Catalysis Using Ruthenium Complexes in Chemical Biology, *Chem. – Eur. J.*, 2019, **25**, 6661–6672.
29 Q. Wang and D. Astruc, State of the Art and Prospects in Metal–Organic Framework (MOF)-Based and MOF-Derived Nanocatalysis, *Chem. Rev.*, 2020, **120**, 1438–1511.
30 C. Vaitsis, G. Sourkouni and C. Argirusis, Metal Organic Frameworks (MOFs) and Ultrasound: A Review, *Ultrason. Sonochem.*, 2019, **52**, 106–119.
31 H. Furukawa, N. Ko, Y. B. Go, N. Aratani, S. B. Choi, E. Choi, A. O. Yazaydin, R. Snurr, M. O'Keeffe, J. Kim and O. M. Yaghi, Ultrahigh Porosity in Metal-Organic Frameworks, *Science*, 2010, **329**, 424–428.
32 H.-C. Zhou, J. R. Long and O. M. Yaghi, Introduction to Metal—Organic Frameworks, *Chem. Rev.*, 2012, **112**, 673–674.
33 M. O'Keeffe and O. M. Yaghi, Deconstructing the Crystal Structures of Metal-Organic Frameworks and Related Materials into Their Underlying Nets, *Chem. Rev.*, 2012, **112**, 675–702.
34 Z. Hu, B. J. Deibert and J. Li, Luminescent Metal—Organic Frameworks for Chemical Sensing and Explosive Detection, *Chem. Soc. Rev.*, 2014, **43**, 5815–5840.
35 H.-C. Zhou and S. Kitagawa, Metal—Organic Frameworks (MOFs), *Chem. Soc. Rev.*, 2014, **43**, 5415–5418.
36 T. Devic and C. Serre, High Valence 3p and Transition Metal Based MOFs, *Chem. Soc. Rev.*, 2014, **43**, 6097–6115.
37 M. Ding, R. W. Flaig, H.-L. Jiang and O. M. Yaghi, Carbon Capture and Conversion Using Metal—Organic

Frameworks and MOF-Based Materials, *Chem. Soc. Rev.*, 2019, **48**, 2783–2828.
38 A. Czaja, N. Trukhan and U. Müller, Industrial Applications of Metal–Organic Frameworks, *Chem. Soc. Rev.*, 2009, **38**, 1284–1293.
39 H. Furukawa, K. E. Cordova, M. O'Keeffe and O. M. Yaghi, The Chemistry and Applications of Metal-Organic Frameworks, *Science*, 2013, **341**, 1230444.
40 G.-L. Yang, X.-L. Jiang, H. Xu and B. Zhao, Applications of MOFs as Luminescent Sensors for Environmental Pollutants, *Small*, 2021, **17**, 2005327.
41 M. Ding, X. Cai and H.-L. Jiang, Improving MOF Stability: Approaches and Applications, *Chem. Sci.*, 2019, **10**, 10209–10230.
42 R. J. Kuppler, D. J. Timmons, Q.-R. Fang, J.-R. Li, T. A. Makal, M. D. Young, D. Yuan, D. Zhao, W. Zhuang and H.-C. Zhou, Potential Applications of Metal-Organic Frameworks, *Coord. Chem. Rev.*, 2009, **253**, 3042–3066.
43 A. Bavykina, N. Kolobov, I. S. Khan, J. A. Bau, A. Ramirez and J. Gascon, Metal–Organic Frameworks in Heterogeneous Catalysis: Recent Progress, New Trends, and Future Perspectives, *Chem. Rev.*, 2020, **120**, 8468–8535.
44 M. Sadakiyo, Support Effects of Metal–Organic Frameworks in Heterogeneous Catalysis, *Nanoscale*, 2022, **14**, 3398–3406.
45 A. Dhakshinamoorthy, M. Opanasenko, J. Čejka and H. Garcia, Metal Organic Frameworks as Heterogeneous Catalysts for the Production of Fine Chemicals, *Catal. Sci. Technol.*, 2013, **3**, 2509–2540.
46 S. R. Halper, L. Do, J. R. Stork and S. M. Cohen, Topological Control in Heterometallic Metal–Organic Frameworks by Anion Templating and Metalloligand Design, *J. Am. Chem. Soc.*, 2006, **128**, 15255–15268.
47 M. Y. Masoomi, A. Morsali, A. Dhakshinamoorthy and H. Garcia, Mixed-Metal MOFs: Unique Opportunities in Metal–Organic Framework (MOF) Functionality and Design, *Angew. Chem., Int. Ed.*, 2019, **58**, 15188–15205.
48 S. Pachisia and R. Gupta, Architectural and catalytic aspects of designer materials built using metalloligands of pyridine- 2,6-dicarboxamide based ligands, *Dalton Trans.*, 2020, **49**, 14731–14748.
49 G. Kumar, G. Kumar and R. Gupta, Effect of Pyridyl Donors from Organic Ligands versus Metalloligands on Material Design, *Inorg. Chem. Front.*, 2021, **8**, 1334–1373.
50 G. Kumar and R. Gupta, Molecularly Designed Architectures–the Metalloligand Way, *Chem. Soc. Rev.*, 2013, **42**, 9403–9453.
51 G. Kumar and R. Gupta, Coordination Driven Architectures Based on Metalloligands Offering Appended Carboxylic Acid Groups, *J. Chem. Sci.*, 2018, 130.
52 R. Gupta, G. Kumar and R. Gupta, Encapsulation-Led Adsorption of Neutral Dyes and Complete Photodegradation of Cationic Dyes and Antipsychotic Drugs by Lanthanide-Based Macrocycles, *Inorg. Chem.*, 2022, **61**, 7682–7699.
53 S. Pachisia and R. Gupta, Tailored Inorganic-Organic Architectures via Metalloligands, *Chem. Rec.*, 2022, **22**, e202200121.
54 L. Zhu, F. Hu, B. Sun, S. Gu, T. Gao and G. Zhou, Recent Advances on Multivariate MOFs for Photocatalytic CO_2 Reduction and H_2 Evolution, *Adv. Sustainable Syst.*, 2023, **7**, 2200394.
55 Z. Lei, Y. Xue, W. Chen, W. Qiu, Y. Zhang, S. Horike and L. Tang, MOFs-Based Heterogeneous Catalysts: New Opportunities for Energy-Related CO_2 Conversion, *Adv. Energy Mater.*, 2018, **8**, 1801587.
56 D. Li, M. Kassymova, X. Cai, S.-Q. Zang and H.-L. Jiang, Photocatalytic CO_2 Reduction over Metal-Organic Framework-Based Materials, *Coord. Chem. Rev.*, 2020, **412**, 213262.
57 W. Zhan, H. Gao, Y. Yang, X. Li and Q.-L. Zhu, Rational Design of Metal–Organic Framework-Based Materials for Photocatalytic CO_2 Reduction, *Adv. Energy Sustainability. Res.*, 2022, **3**, 2200004.
58 R. Gupta, Aashish, Upma, S. Majumdar, P. K. Chowdhury and R. Gupta, Visible light mediated photocatalysis by lanthanide metal–organic frameworks: enhanced specificity and mechanistic insights, *Chem. Sci.*, 2024, **15**, 18952–18968.
59 L. Li, S. Zhang, L. Xu, J. Wang, L.-X. Shi, Z.-N. Chen, M. Hong and J. Luo, Effective Visible-Light Driven CO_2 Photoreduction via a Promising Bifunctional Iridium Coordination Polymer, *Chem. Sci.*, 2014, **5**, 3808–3813.
60 K. Fan, W.-X. Nie, L.-P. Wang, C.-H. Liao, S.-S. Bao and L.-M. Zheng, Defective Metal–Organic Frameworks Incorporating Iridium-Based Metalloligands: Sorption and Dye Degradation Properties, *Chem. – Eur. J.*, 2017, **23**, 6615–6624.
61 R. Gupta, S. A. Ali, Upma, T. Ahmad and R. Gupta, Unprecedented Hydrogen Evolution Reactions Based on the Accelerating Effect of [Co–Tb]-Supramolecular Complex-Anchored CdS Heterojunctions, *ACS Appl. Mater. Interfaces*, 2025, **17**, 28244–28255.
62 Upma, K. Boora, R. Gupta and R. Gupta, Visible Light Catalyzed Oxidative Reactions Using Silver-Based Metal–Organic Frameworks Based on Metalloligands, *Inorg. Chem.*, 2025, **64**, 10624–10636.
63 S. Zhang, L. Li, S. Zhao, Z. Sun and J. Luo, Construction of Interpenetrated Ruthenium Metal-Organic Frameworks as Stable Photocatalysts for CO_2 Reduction, *Inorg. Chem.*, 2015, **54**, 8375–8379.
64 G. Lan, Z. Li, S. S. Veroneau, Y.-Y. Zhu, Z. Xu, C. Wang and W. Lin, Photosensitizing Metal–Organic Layers for Efficient Sunlight-Driven Carbon Dioxide Reduction, *J. Am. Chem. Soc.*, 2018, **140**, 12369–12373.
65 S. Chen, K. Li, F. Zhao, L. Zhang, M. Pan, Y.-Z. Fan, J. Guo, J. Shi and C.-Y. Su, A Metal-Organic Cage Incorporating Multiple Light Harvesting and Catalytic Centres for Photochemical Hydrogen Production, *Nat. Commun.*, 2016, **7**, 13169.
66 O. S. Wenger, Photoactive Complexes with Earth-Abundant Metals, *J. Am. Chem. Soc.*, 2018, **140**, 13522–13533.

67 X. Feng, Y. Pi, Y. Song, Z. Xu, Z. Li and W. Lin, Integration of Earth-Abundant Photosensitizers and Catalysts in Metal–Organic Frameworks Enhances Photocatalytic Aerobic Oxidation, *ACS Catal.*, 2021, **11**, 1024–1032.
68 M. S. Deenadayalan, N. Sharma, P. K. Verma and C. M. Nagaraja, Visible-Light-Assisted Photocatalytic Reduction of Nitroaromatics by Recyclable Ni(II)-Porphyrin Metal–Organic Framework (MOF) at RT, *Inorg. Chem.*, 2016, **55**, 5320–5327.
69 X.-Y. Zhang, C.-F. Xie, S.-Q. Wang, X.-M. Chang, Y. Zhang, Y. Zhao, Y. Lu and W.-Y. Sun, Coordination Polymers with 2,2′:6′,2″-Terpyridine Earth-Abundant Metal Complex Units for Selective CO_2 Photoreduction, *Inorg. Chem.*, 2022, **61**, 1590–1596.
70 S. Zhang, L. Han, L. Li, J. Cheng, D. Yuan and J. A. Luo, Highly Symmetric Metal–Organic Framework Based on a Propeller-Like Ru-Organic Metalloligand for Photocatalysis and Explosives Detection, *Cryst. Growth Des.*, 2013, **13**, 5466–5472.
71 M. Ballico, D. Alessi, C. Jandl, D. Lovison and W. Baratta, Terpyridine Diphosphine Ruthenium Complexes as Efficient Photocatalysts for the Transfer Hydrogenation of Carbonyl Compounds, *Chem. – Eur. J.*, 2022, **28**, e202201722.
72 Y. Kuramochi, O. Ishitani and H. Ishida, Reaction Mechanisms of Catalytic Photochemical CO_2 Reduction Using Re(I) and Ru(II) Complexes, *Coord. Chem. Rev.*, 2018, **373**, 333–356.
73 J. Huo, Y.-B. Zhang, W.-Y. Zou, X. Hu, Q. Deng and D. Chen, Mini-Review on an Engineering Approach towards the Selection of Transition Metal Complex-Based Catalysts for Photocatalytic H_2 Production, *Catal. Sci. Technol.*, 2019, **9**, 2716–2727.
74 D. N. Tritton, F.-K. Tang, G. B. Bodedla, F.-W. Lee, C.-S. Kwan, K. Leung, C.-F. Zhu and W.-Y. Wong, Development and Advancement of Iridium(III)-Based Complexes for Photocatalytic Hydrogen Evolution, *Coord. Chem. Rev.*, 2022, **459**, 214390.
75 S. K. Loeb, P. J. J. Alvarez, J. A. Brame, E. L. Cates, W. Choi, J. Crittenden, D. D. Dionysiou, Q. Li, G. Li-Puma, X. Quan, D. L. Sedlak, T. David Waite, P. Westerhoff and J.-H. Kim, The Technology Horizon for Photocatalytic Water Treatment: Sunrise or Sunset?, *Environ. Sci. Technol.*, 2019, **53**, 2937–2947.
76 K. M. Lee, C. W. Lai, K. S. Ngai and J. C. Juan, Recent Developments of Zinc Oxide Based Photocatalyst in Water Treatment Technology: A Review, *Water Res.*, 2016, **88**, 428–448.
77 C.-C. Wang, J.-R. Li, X.-L. Lv, Y.-Q. Zhang and G. Guo, Photocatalytic Organic Pollutants Degradation in Metal–Organic Frameworks, *Energy Environ. Sci.*, 2014, **7**, 2831–2867.
78 G. Sriram, A. Bendre, E. Mariappan, T. Altalhi, M. Kigga, Y. C. Ching, H.-Y. Jung, B. Bhaduri and M. Kurkuri, Recent Trends in the Application of Metal-Organic Frameworks (MOFs) for the Removal of Toxic Dyes and Their Removal Mechanism-a Review, *Sustainable Mater. Technol.*, 2022, **31**, e00378.
79 S. Rojas and P. Horcajada, Metal–Organic Frameworks for the Removal of Emerging Organic Contaminants in Water, *Chem. Rev.*, 2020, **120**, 8378–8415.
80 R. S. Kookana, P. Drechsel, P. Jamwal and J. Vanderzalm, Urbanisation and Emerging Economies: Issues and Potential Solutions for Water and Food Security, *Sci. Total Environ.*, 2020, **732**, 139057.
81 M. C. M. Van Loosdrecht and D. Brdjanovic, Anticipating the next Century of Wastewater Treatment, *Science*, 2014, **344**, 1452–1453.
82 K. R. Davies, Y. Cherif, G. P. Pazhani, S. Anantharaj, H. Azzi, C. Terashima, A. Fujishima and S. Pitchaimuthu, The Upsurge of Photocatalysts in Antibiotic Micropollutants Treatment: Materials Design, Recovery, Toxicity and Bioanalysis, *J. Photochem. Photobiol.*, 2021, **48**, 100437.
83 M. Mon, R. Bruno, J. Ferrando-Soria, D. Armentano and E. Pardo, Metal–Organic Framework Technologies for Water Remediation: Towards a Sustainable Ecosystem, *J. Mater. Chem. A*, 2018, **6**, 4912–4947.
84 A. Wankhade, Removal of Organic Pollutant from Water by Heterogenous Photocatalysis: A Review, *Res. J. Chem. Environ.*, 2013, 1784.
85 K. Kabra, R. Chaudhary and R. L. Sawhney, Treatment of Hazardous Organic and Inorganic Compounds through Aqueous-Phase Photocatalysis: A Review, *Ind. Eng. Chem. Res.*, 2004, **43**, 7683–7696.
86 R. Gothwal and T. Shashidhar, Antibiotic Pollution in the Environment: A Review, *Clean:Soil, Air, Water*, 2015, **43**, 479–489.
87 M. J. F. Calvete, G. Piccirillo, C. S. Vinagreiro and M. M. Pereira, Hybrid Materials for Heterogeneous Photocatalytic Degradation of Antibiotics, *Coord. Chem. Rev.*, 2019, **395**, 63–85.
88 P. A. K. Reddy, P. V. L. Reddy, E. Kwon, K.-H. Kim, T. Akter and S. Kalagara, Recent Advances in Photocatalytic Treatment of Pollutants in Aqueous Media, *Environ. Int.*, 2016, **91**, 94–103.
89 C. Zamora-Ledezma, D. Negrete-Bolagay, F. Figueroa, E. Zamora-Ledezma, M. Ni, F. Alexis and V. H. Guerrero, Heavy Metal Water Pollution: A Fresh Look about Hazards, Novel and Conventional Remediation Methods, *Environ. Technol. Innovation*, 2021, **22**, 101504.
90 M. E. Ali, M. Ullah and S. B. A. Hamid, Conventional to Nano-Green Adsorbents for Water Pollution Management, A Review, *Adv. Mater. Res.*, 2014, **925**, 674–678.
91 W. Ying, W. Zhang, Q. Chang, W. Jiang and G. Li, Improved Methods for Carbon Adsorption Studies for Water and Wastewater Treatment, *Environ. Prog.*, 2006, **25**, 110–120.
92 B. Wang, X.-L. Lv, D. Feng, L.-H. Xie, J. Zhang, M. Li, Y. Xie, J.-R. Li and H.-C. Zhou, Highly Stable Zr(IV)-Based Metal–Organic Frameworks for the Detection and Removal of Antibiotics and Organic Explosives in Water, *J. Am. Chem. Soc.*, 2016, **138**, 6204–6216.

93 K. K. Sodhi, M. Kumar, B. Balan, A. S. Dhaulaniya, P. Shree, N. Sharma and D. K. Singh, Perspectives on the antibiotic contamination, resistance, metabolomics, and systemic remediation, *SN Appl. Sci.*, 2021, **3**, 269.
94 A. L. Batt, S. Kim and D. S. Aga, Comparison of the occurrence of antibiotics in four full-scale wastewater treatment plants with varying designs and operations, *Chemosphere*, 2007, **68**, 428–435.
95 J. Wang and R. Zhuan, Degradation of Antibiotics by Advanced Oxidation Processes: An Overview, *Sci. Total Environ.*, 2020, **701**, 135023.
96 Y. Jiang, J. Ran, K. Mao, X. Yang, L. Zhong, C. Yang, X. Feng and H. Zhang, Recent Progress in Fenton/Fenton-like Reactions for the Removal of Antibiotics in Aqueous Environments, *Ecotoxicol. Environ. Saf.*, 2022, **236**, 113464.
97 M. Z. Akbari, Y. Xu, Z. Lu and L. Peng, Review of Antibiotics Treatment by Advance Oxidation Processes, *Environ. Adv.*, 2021, **5**, 100111.
98 M. Brienza and I. Katsoyiannis, Sulfate Radical Technologies as Tertiary Treatment for the Removal of Emerging Contaminants from Wastewater, *Sustainability*, 2017, **9**, 1604.
99 J. H. Burness, J. G. Dillard and L. T. Taylor, X-ray photoelectron spectroscopic study of cobalt(II) Schiff base complexes and their oxygenation products, *J. Am. Chem. Soc.*, 1975, **97**, 6080–6088.
100 J. Cañón and A. V. Teplyakov, XPS Characterization of Cobalt Impregnated SiO_2 and γ-Al_2O_3, *Surf. Interface Anal.*, 2021, **53**, 475–481.
101 K. Nakamoto, *Infrared and Raman Spectra of Inorganic and Coordination compounds: Part A: Theory and Applications in Inorganic Chemistry*, John Wiley & Sons, Inc., 6th edn, 2008.
102 K. Nakamoto, *Infrared and Raman Spectra of Inorganic and Coordination compounds: Part B: Theory and Applications in Inorganic Chemistry*, John Wiley & Sons, Inc., 6th edn, 2008.
103 J. Zou, C. Fan, Y. Jiang, X. Liu, W. Zhou, H. Xu and L. A. Huang, Preliminary Study on Assessing the Brunauer-Emmett-Teller Analysis for Disordered Carbonaceous Materials, *Microporous Mesoporous Mater.*, 2021, **327**, 111411.
104 F. Ambroz, T. J. Macdonald, V. Martis and I. P. Parkin, Evaluation of the BET Theory for the Characterization of Meso and Microporous MOFs, *Small Methods*, 2018, **2**, 1800173.
105 S. Pachisia and R. Gupta, Supramolecular Catalysis: The Role of H-Bonding Interactions in Substrate Orientation and Activation, *Dalton Trans.*, 2021, **50**, 14951–14966.
106 C. A. Hunter, Quantifying Intermolecular Interactions: Guidelines for the Molecular Recognition Toolbox, *Angew. Chem., Int. Ed.*, 2004, **43**, 5310–5324.
107 E. Persch, O. Dumele and F. Diederich, Molecular Recognition in Chemical and Biological Systems, *Angew. Chem., Int. Ed.*, 2015, **54**, 3290–3327.
108 S. Navalón, A. Dhakshinamoorthy, M. Álvaro, B. Ferrer and H. García, Metal–Organic Frameworks as Photocatalysts for Solar-Driven Overall Water Splitting, *Chem. Rev.*, 2023, **123**, 445–490.
109 M. I. Hutchings, A. W. Truman and B. Wilkinson, Antibiotics: Past, Present and Future, *Curr. Opin. Microbiol.*, 2019, **51**, 72–80.
110 C. Zhao, M. Pelaez, X. Duan, H. Deng, K. O'Shea, D. Fatta-Kassinos and D. D. Dionysiou, Role of pH on Photolytic and Photocatalytic Degradation of Antibiotic Oxytetracycline in Aqueous Solution under Visible/Solar Light: Kinetics and Mechanism Studies, *Appl. Catal., B*, 2013, **134–135**, 83–92.
111 J. Wei, T. Fang and M. Shiraiwa, Effects of Acidity on Reactive Oxygen Species Formation from Secondary Organic Aerosols, *ACS Environ. Au*, 2022, **2**, 336–345.
112 Y. Wen, M. Feng, P. Zhang, H.-C. Zhou, V. K. Sharma and X. Ma, Metal Organic Frameworks (MOFs) as Photocatalysts for the Degradation of Agricultural Pollutants in Water, *ACS ES&T Eng.*, 2021, **1**, 804–826.
113 Z. Zhang, Y. Liang, H. Huang, X. Liu, Q. Li, L. Chen and D. Xu, Stable and Highly Efficient Photocatalysis with Lead-Free Double-Perovskite of $Cs_2AgBiBr_6$, *Angew. Chem., Int. Ed.*, 2019, **58**, 7263–7267.
114 T. Xia, Y. Lin, W. Li and M. Ju, Photocatalytic Degradation of Organic Pollutants by MOFs Based Materials: A Review, *Chin. Chem. Lett.*, 2021, **32**, 2975–2984.
115 J. Zhang, S. Xiang, P. Wu, D. Wang, S. Lu, S. Wang, F. Gong, X. Wei, X. Ye and P. Ding, Recent Advances in Performance Improvement of Metal-Organic Frameworks to Remove Antibiotics: Mechanism and Evaluation, *Sci. Total Environ.*, 2022, **811**, 152351.
116 S. R. Labhade and V. B. Gaikwad, Spectrophotometric Determination of Fluoride Using Ferric-Thiocyanate Absorbing System, *Asian J. Chem.*, 2009, **21**, 7117–7124.
117 W. Gao, J. Lu, S. Zhang, X. Zhang, Z. Wang, W. Qin, J. Wang, W. Zhou, H. Liu and Y. Sang, Suppressing Photoinduced Charge Recombination via the Lorentz Force in a Photocatalytic System, *Adv. Sci.*, 2019, **6**, 1901244.
118 C. Pan, J. Xu, Y. Wang, D. Li and Y. Zhu, Dramatic Activity of C_3N_4/$BiPO_4$ Photocatalyst with Core/Shell Structure Formed by Self-Assembly, *Adv. Funct. Mater.*, 2012, **22**, 1518–1524.
119 C. Ruckebusch, M. Sliwa, P. Pernot, A. de Juan and R. Tauler, Comprehensive Data Analysis of Femtosecond Transient Absorption Spectra, A Review, *J. Photochem. Photobiol.*, 2012, **13**, 1–27.
120 T. J. Miao and J. Tang, Characterization of Charge Carrier Behavior in Photocatalysis Using Transient Absorption Spectroscopy, *J. Chem. Phys.*, 2020, **152**, 194201.
121 R. Berera, R. Van Grondelle and J. T. M. Kennis, Ultrafast Transient Absorption Spectroscopy: Principles and Application to Photosynthetic Systems, *Photosynth. Res.*, 2009, **101**, 105–118.
122 J. Li and N. Wu, Semiconductor-Based Photocatalysts and Photoelectrochemical Cells for Solar Fuel Generation: A Review, *Catal. Sci. Technol.*, 2015, **5**, 1360–1384.

123 B. Athokpam, S. G. Ramesh and R. H. McKenzie, Effect of Hydrogen Bonding on the Infrared Absorption Intensity of OH Stretch Vibrations, *Chem. Phys.*, 2017, **488–489**, 43–54.

124 B. Bhongade, S. Talath and S. A. Dhaneshwar, Validated Method for the Quantitation of Ciprofloxacin Hydrochloride Using Diffuse Reflectance Infrared Fourier Transform Spectroscopy, *Int. J. Spectrosc.*, 2014, **2014**, e294612.

125 S. Pandey, P. Pandey, G. Tiwari, R. Tiwari and A. K. Rai, FTIR Spectroscopy: A Tool for Quantitative Analysis of Ciprofloxacin in Tablets, *Indian J. Pharm. Sci.*, 2012, **74**, 86.

126 G. Kumar, S. Pachisia, P. Kumar, V. Kumar and V. Gupta, Zn- and Cd-Based Coordination Polymers Offering H-Bonding Cavities: Highly Selective Sensing of $S_2O_7^{2-}$ and Fe^{3+} Ions, *Chem. – Asian J.*, 2019, **14**, 4594–4600.

127 M. Prashad, D. Har, B. Hu, H.-Y. Kim, O. Repic and T. J. Blacklock, An Efficient and Practical N-Methylation of Amino Acid Derivatives, *Org. Lett.*, 2003, **5**, 125–128.

128 S. Palaniappan and M. Ram, Esterification of Carboxylic Acids with Alcohols Catalyzed by Polyaniline Salts, *Green Chem.*, 2002, **4**, 53–55.

129 S. P. Tripathy, S. Subudhi, A. Ray, P. Behera, A. Bhaumik and K. Parida, Mixed-Valence Bimetallic Ce/Zr MOF-Based Nanoarchitecture: A Visible-Light-Active Photocatalyst for Ciprofloxacin Degradation and Hydrogen Evolution, *Langmuir*, 2022, **38**, 1766–1780.

130 A. Chatterjee, A. K. Jana and J. K. Basu, A Binary MOF of Iron and Copper for Treating Ciprofloxacin-Contaminated Waste Water by an Integrated Technique of Adsorption and Photocatalytic Degradation, *New J. Chem.*, 2021, **45**, 17196–17210.

131 A. Verma, S. Kumar and Y.-P. Fu, A Ternary-Hybrid as Efficiently Photocatalytic Antibiotic Degradation and Electrochemical Pollutant Detection, *J. Chem. Eng.*, 2021, **408**, 127290.

132 X. Lu, Y. Wang, X. Zhang, G. Xu, D. Wang, J. Lv, Z. Zheng and Y. Wu, NiS and MoS_2 Nanosheet Co-Modified Graphitic C_3N_4 Ternary Heterostructure for High Efficient Visible Light Photodegradation of Antibiotic, *J. Hazard. Mater.*, 2018, **341**, 10–19.

133 J. Xue, S. Ma, Y. Zhou and Q. Wang, Au-Loaded Porous Graphitic C_3N_4/Graphene Layered Composite as a Ternary Plasmonic Photocatalyst and Its Visible-Light Photocatalytic Performance, *RSC Adv.*, 2015, **5**, 88249–88257.

134 Y. Chen, C. Hu, J. Qu and M. Yang, Photodegradation of Tetracycline and Formation of Reactive Oxygen Species in Aqueous Tetracycline Solution under Simulated Sunlight Irradiation, *J. Photochem. Photobiol., A*, 2008, **197**, 81–87.

135 C. Wang, Y. Xiao, Q. Li, J. Den and K. Wang, Free Radicals, Apparent Activation Energy, and Functional Groups during Low-Temperature Oxidation of Jurassic Coal in Northern Shaanxi, *Int. J. Min. Sci. Technol.*, 2018, **28**, 469–475.

136 E. T. Denisov, Free Radical Addition: Factors Determining the Activation Energy, *Russ. Chem. Rev.*, 2000, **69**, 153–164.

137 M. Hayyan, M. A. Hashim and I. M. AlNashef, Superoxide Ion: Generation and Chemical Implications, *Chem. Rev.*, 2016, **116**, 3029–3085.

138 A. Phaniendra, D. B. Jestadi and L. Periyasamy, Free Radicals: Properties, Sources, Targets, and Their Implication in Various Diseases, *Indian J. Clin. Biochem.*, 2015, **30**, 11.

139 F. Collin, Chemical Basis of Reactive Oxygen Species Reactivity and Involvement in Neurodegenerative Diseases, *Int. J. Mol. Sci.*, 2019, 20.

140 C. Zhang, Y. Wu, D. Li and H.-L. Jiang, Recent advances in MOF composites for photocatalysis, *Chem. Sci.*, 2025, **16**, 13149–13172.

141 (*a*) CCDC 2485439: Experimental Crystal Structure Determination, 2025, DOI: **10.5517/ccdc.csd.cc2pf9gx**; (*b*) CCDC 2485440: Experimental Crystal Structure Determination, 2025, DOI: **10.5517/ccdc.csd.cc2pf9hy**.

